TECHNISCHE UNIVERSITÄT WIEN

Diploma Thesis

Optimization of Electric Field Microsensor Design based on FEM Simulations

Institute of Sensor and Actuator Systems
Vienna University of Technology

under the supervision of

Ao. Univ.Prof. Dipl.Ing. Dr.techn. Franz Keplinger
Dipl.Ing. Andreas Kainz

and

Dipl.Ing. Dr.techn. Wilfried Hortschitz

October 27, 2016

by

Georg Traxler, BSc.
1126049

Statutory Declaration

I declare that I have authored this thesis independently, that I have not used other than the declared sources/resources, and that I have explicitly marked all material which has been quoted either literally or by content from the used sources.

Vienna, ______________________ ______________________

Date Signature

Eidesstattliche Erklärung[1]

Ich erkläre an Eides statt, dass ich die vorliegende Arbeit selbstständig verfasst, andere als die angegebenen Quellen/Hilfsmittel nicht benutzt, und die den benutzten Quellen wörtlich und inhaltlich entnommenen Stellen als solche kenntlich gemacht habe.

Wien, am ______________________ ______________________

Datum Unterschrift

[1] Beschluss der Curricula-Kommission für Bachelor-, Master- und Diplomstudien vom 10.11.2008; Genehmigung des Senates am 1.12.2008

Abstract

In modern life, magnetic sensors are widely spread and based on many different principles. The miniaturized types like the GMR were first developed only for hard disk drives but triggered science applications in biology and medicine where they, e.g., allow detecting magnetic nano- and microbeads that are labeled with specific antibodies. In contrast to this, one can hardly find any electric field sensors. This is mainly because sensors need electrical conducting leads that disturb dramatically the electric field. The existing electric field sensors are limited in their applications due to their large and complex mechanical configurations. This lack of sensors is responsible for the insufficient knowledge about the interaction of electric fields with organisms or about their generation of fields. The treated novel electric field sensing principle uses micro-electro-mechanical systems (MEMS) technology with an optical readout to achieve a very small device that will enable mobile and precise measurements. At the end, this sensor will allow devices that could warn against thunderstorms or electrostatic discharges, and measure electric fields caused by animals and plants. Within the scope of this diploma thesis, the design of the MEMS transducer is optimized in order to maximize the sensitivity to electric fields and to minimize the risk of failure during the fabrication. Based on FEM simulations, various important characteristics are found and considered in the development of new chip designs. The novel geometries are implemented into the existing Python-code for generating the lithography masks of the individual layers. The fabrication of the new designs revealed further problems which should be considered in the development of the next chip generations.

Contents

1 Introduction to Electric Field Sensors

This chapter shows the motivations for electric field sensors, state-of-the-art instruments and the novel electric field sensing principle. The content of this chapter partly follows the proposal of an FWF project („Fond zur Förderung der wissenschaftlichen Forschung“). [1].

1.1 Electric Fields in Atmosphere

It is assumed that thunderstorms play a major role as generators in the so-called global atmospheric electric circuit (GEC). The structure of the GEC is afforded by a thin insulating layer of atmosphere which is sandwiched between the conductive Earth and the conductive ionosphere [2]. The ionosphere is a region of Earth's upper atmosphere from about 60 to 1000 kilometers altitude which is ionized by solar radiation and filled with hot and dense plasma [3]. In fair weather, the net charge is positive and at heights of about 80 km the electric potential of the ionosphere (electrosphere) is approximately 300 kV [4]. Between the negatively charged Earth's surface and the positively charged ionosphere, a fair-weather electric field of about 100 V/m is observed at ground level [2]. There are various complex processes occurring in the GEC, which are illustrated in Fig. 1.1. The details of many of these, however, are hardly known.

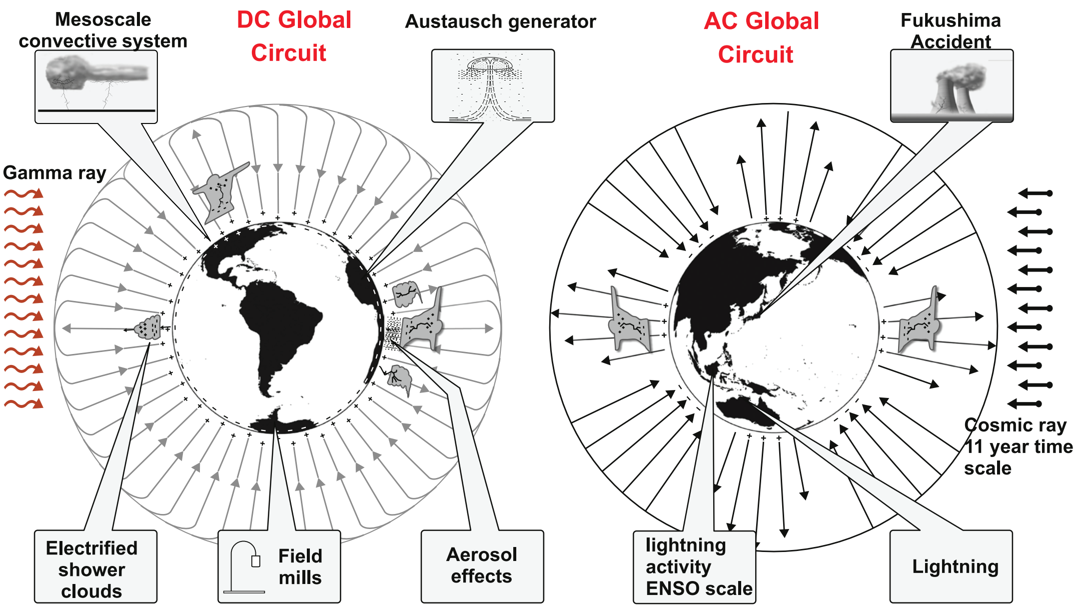

Figure 1.1: Diagram of the global electric circuit for AC and DC components [2].

In general, the diurnal variations of the GEC are maintained by the electrified moist convection worldwide. Major contributors to the charging of the GEC are thunderstorms and electrified shower clouds but there is still no agreement on how thunderstorms, for instance, induce charge separation. The thunder activity has a major influence on the diurnal variations of the GEC: The electric charge within a thundercloud produces an electrostatic field of about 10 kV/m on the ground which is usually much larger than fair-weather electric fields of around 100 V/m. Therefore, measuring the electric field of a thunderstorm, as it develops or approaches, represents an element for early thunderstorm warning. By measuring the field changes at several sites simultaneously, the centroid of the lightning-caused change in the cloud charge can be located because cloud-ground and intra-cloud lightnings generate abrupt changes in the electrostatic field. Nevertheless, it is still a big challenge to determine the charging mechanisms of thunderstorms and the initiation of the lightning discharge itself. For example, this information would be important for forecasters when an electric charge might trigger lightning during the launch of a space craft. There are still many open questions in lightning research depending on the knowledge of the local electric field before and during the thunderstorm.

The alterations in the ionospheric layers between day and night and the varying production of aerosol and particulate pollution on Earth's surface lead to further GEC changes [4]. In general, air pollution decreases the electrical conductivity and increases the electric field. For example, potential gradient measurements in cities have shown peak values in the rush hour. In order to measure the field uncontaminated by pollution, electric field measurements have to be performed on mountain-tops, at sea, by using air-balloons or high-flying air-craft. On the other hand, electrical measurements can be considered as indicators of air pollution.

An interesting observation was made by Takeda [5]: After the Fukushima Dai-ichi nuclear power plant released a massive amount of radioactive material on 14 March 2011, the vertical atmospheric electric field at ground level dropped by one order of magnitude at a location 150 km southwest of the plant. The reason for the potential gradient drop is the ionization effect of radioactive materials. Thus, a network of high-temporal resolution electric field observations surrounding the nuclear power plant is one good monitor of the radioactive dust cloud, providing independent information from radiation dose measurements.

1.2 State-of-the-art

As the measurement of static, quasi-static and low frequency electric fields (E-fields) is so important, for example for meteorology or space survey, different E-field measurement principles have been developed over the last decades. Only a short review of the state-of-the-art is given in this chapter.

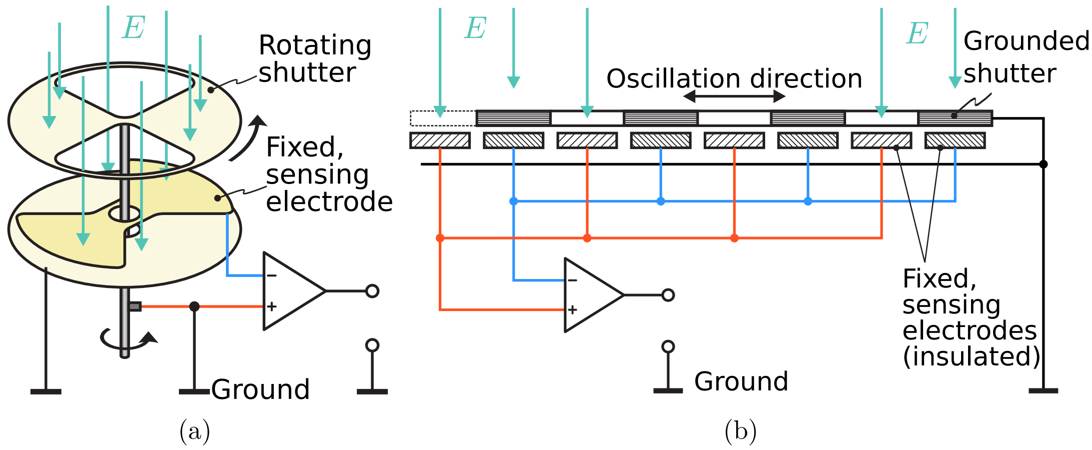

Figure 1.2: (a) Working principle of electric field mills: The insulated vanes representing the sensing electrode is periodically exposed to and shielded from the electric field by the grounded, rotating shutter [1]. (b) Basic concept of MEMS electric field mills [1].

1.2.1 Direct Electrical Measurements

In direct electrical measurements, the E-field charges up conducting surfaces via electrostatic induction or deflects locally free electrons. For example, Roncin et. al. developed an E-field sensor which uses a micro-spring supported membrane as the sensing element [6]. The sensing mechanism involves electrostatic forces to deflect the membrane but highly sophisticated electronics are necessary for the readout.

The most common approach to measure E-fields are electric field mills which are illustrated in Fig. 1.2a [7]: Due to a grounded, rotating shutter the insulated, sensing electrode is periodically exposed to and shielded from the electric field. The amount of induced charge q and, hence, the changing output voltage is proportional to the electric field. As conventional field mills are relatively bulky, there have been attempts to miniaturize the field mill concept by using micro-electro-mechanical systems (MEMS) [8, 9, 10, 11]. Rotating field mills are difficult to miniaturize so that one possible actuaction method is to use an oscillating shutter instead of a rotating one (see Fig. 1.2b). For example, Horenstein et. al. developed a micromachined electric field mill which consists of a single slit shutter and a comb drive to actuate the shutter [12]. However, all field mills require grounded electrodes to shield the sensing electrodes from the external electric field. Within the scope of this diploma thesis, it will be shown that this grounded connection leads to an inherent, significant distortion of the electric field and that the measurement of electric fields, in general, is hardly possible without interference by the measurement device. Dielectric bodies develop surface charges and cause small field changes, while conductors lead to much more severe distortions of the electric field which is illustrated in Fig. 1.3. This effect is even more pronounced, when parts of the sensor are grounded which is the case for electric field mills.

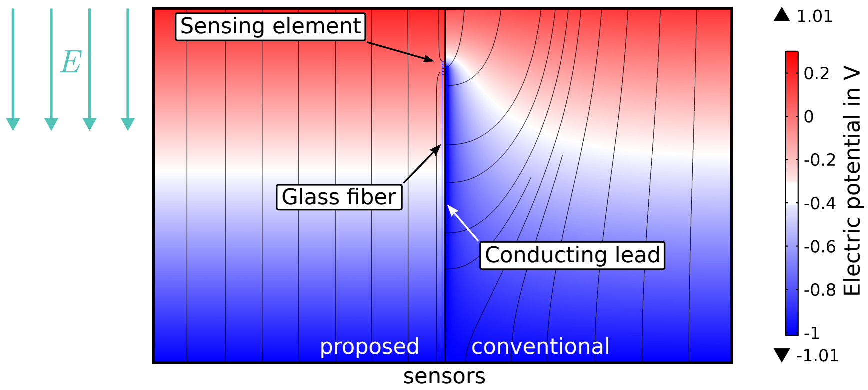

Figure 1.3: Distribution of the electric potential around a dielectric sensor on the left side and around a conductive sensor on the right side [1].

1.2.2 Electro-optic Transduction

Electro-optical systems do not require grounded parts of the sensor or free charges and, hence, represent a superior principle [13]. In general, electro-optically active crystals change their refractive index due to an external E-field according to the equation

$$n(E) = n_0 + S_1 \cdot E + S_2 \cdot E^2, \tag{1.1}$$

where n_0 is the zero-field refractive index and the proportional factors S_1 and S_2 are explained subsequently.

The linear electro-optic effect, also called Pockels effect, refers to changes of the medium refractive index which are proportional to the electric field strength with the proportional factor $S_1 = -\frac{1}{2}{n_0}^2 r_{\text{eff}}$, where r_{eff} is the electro-optic tensor. This effect has been used in many optical sensors due to its high sensitivities for electric fields. For example, Miki et. al. measured electric fields near triggered lightning channels using Pockels sensors [14]. The quadratic electro-optic effect, also called the Kerr effect, refers to changes of the medium refractive index which are proportional to the square of the electric field strength with the proportional factor $S_2 = \lambda K$, where λ is the wavelength of the light and K is the Kerr constant. As this effect is relatively small, the related sensors only work in high E-field magnitudes [15]. Rose et. al. used polarimetric and interferometric Sagnac optical fiber current sensors to determine the electric field.

Electro-optic transducers suffer from the pyro-electric effect which describes the ability of a material to generate a temporary electric field, when it is cooled or heated [16]. As a consequence, temperature variations lead to an additional E-field which distorts the E-field to be quantified. There are various ways and ideas to compensate the intrinsic temperature interference by the electro-optic transducers but no practical sensors have been developed yet, where this problem is satisfyingly solved [17].

1.2.3 Motivation for a New Sensing Concept

In a nutshell, the described state-of-the-art instruments for E-field quantification have some disadvantages: Field mills need a grounded electrode or grounded shielding which massively distorts the E-field. Furthermore, electrical power supply is necessary for long-term operation. The major drawback of electro-optic transducers is the inherent temperature dependence of the optical material. Electric field measurements in meteorology are important not only for early thunderstorm warnings, but also for lightning and geophysical research. On the one hand, the sensor should cause minimum distortions of the E-field, on the other hand, it should be miniaturized and portable. This would make the sensor available even for the average consumer und would trigger a quantum leap of the usability of E-field quantification. In modern life, magnetic sensors are widely spread and based on many different principles. The miniaturized types like the GMR were first developed not only for hard disk drives but triggered science applications in biology and medicine where they, e.g., allow the detection of nano- and microbeads that are labeled with specific antibodies. In contrast to this, one can hardly find any electrical field sensors in biology and medicine as the existing ones are limited in their applications due to their large and complex mechanical configurations. The lack of E-field sensors is responsible for the insufficient knowledge about interactions of electric fields with organisms or about their generation of the fields. The sensor could allow devices that warn against thunderstorms or electrostatic discharges, and measure electric fields caused by animals or plants.

1.3 Novel Electric Field Sensing Principle

The novel electric field sensing principle should establish a new way of passive electric field transduction which promises not only minimum distortion of the electric field but also an improvement in usability of E-field measurements.

1.3.1 Basic Concept of Electric Field Microsensor

In general, the electric field microsensor consists of three functional components:

- An electro-mechanical transducer which transforms the E-field into a mechanical deflection of a MEMS structure.
- An optical readout which converts the mechanical deflection into an intensity modulated optical signal.
- The optoelectronic components of light source and converter for the received optical intensity into an electrical signal.

Within the scope of this diploma thesis, it will be shown that an external electric field exerts opposite mechanical forces on electrically connected conductors. For insulated conductors, the net force is attractive. These two processes define the electro-mechanical forces which act on the different parts of the MEMS transducer and consequently determine the mechanical deflection resulting from the external electric field. These tiny mechanical deflections can be measured by a MEMS optical flux modulator [18]. The light flux coming from an LED is guided to the MEMS transducer via glass fibers and is then modulated by the relative in-plane movement of two parallel arrays of apertures. The transmitted light flux, which depends on the shading by both apertures, is guided, again via glass fibers, to a phototransistor or photodiode. A schematic cross-section of the sensing element is illustrated in Fig. 1.4.

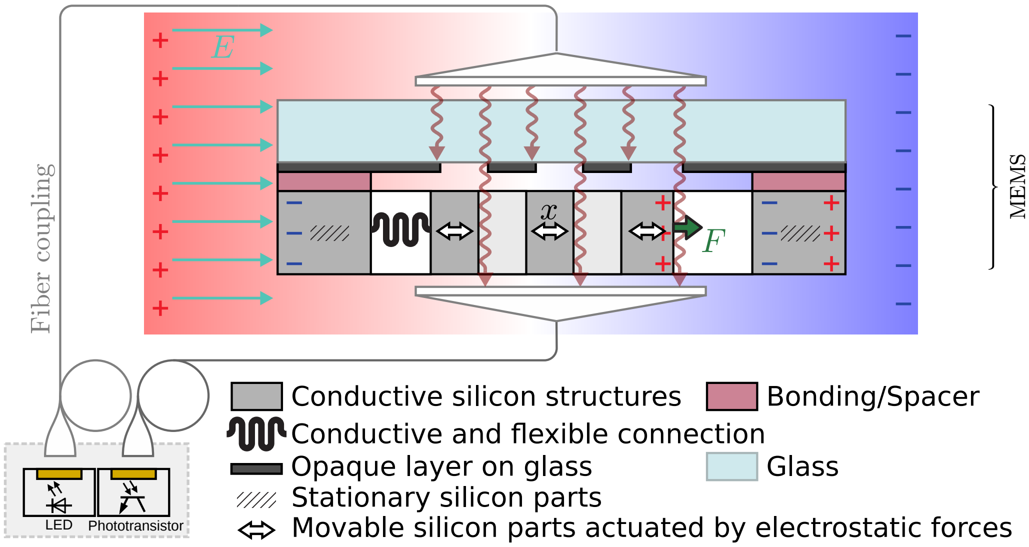

Figure 1.4: Schematic cross-section of the electric field sensing element. The light flux coming from the LED is guided via glass fibers and modulated by two microstructured gratings. The output signal of the phototransistor (or photodiode) depends on the deflection of the movable aperture [1].

1.3.2 Beneficial Characteristics of Novel Electric Field Sensing Principle

The described sensing concept exhibits the following beneficial properties:

- Due to the optical readout, the MEMS transducer is an entirely passive component as the mechanical actuation is only caused by the E-field.
- The field distortion is minimal because the transducer does not need any conductive connections to external objects. By using the optical readout with glass fibers, it is galvanically separated from the optoelectronic components.
- Due to the small dimensions of the MEMS transducer, all induced fields which result from electrostatic induction and dielectric polarization acting on conducting and dielectric constituents of the transducer, respectively, are confined to the vicinity of the transducer and lead only to minor distortions of the electric field.

- The complete transduction chain is not sensitive to temperature variations. While the temperature dependence of the MEMS is small and systematic, the LED, phototransistors and photodiodes can be operated at fixed temperatures.

1.3.3 Fabrication

The fabrication process for the MEMS components is based on silicon on insulator (SOI) technology and illustrated in Fig. 1.5. The SOI wafer consists of a 250 µm thick silicon handle layer, an intermediate SiO_2 with a thickness of 1 μmm and a 45μmm thick silicon device layer. At first, the microstructures including the first aperture array are formed (see Fig. 1.5a): For this, positive photolithography is applied to yield a pattern of photoresist covering the device layer. The uncovered regions of the device layer are removed by Bosch Deep Reactive Ion Etching (DRIE). Then a protective photoresist is applied to cover the structures during the following process where the supporting handle layer is partly removed beneath the microstructures by a further plasma etching process (see Fig. 1.5b). Afterwards, wet etching removes the remaining SiO_2 intermediate layer and releases the movable microstructures in the device layer which is illustrated in Fig. 1.5c. After stripping the protective layer, a 520 µm thick glass wafer with the second aperture array made of chrome is bonded onto the top side of the SOI wafer with SU-8 as bonding adhesive (see Fig. 1.5d). Prior to the bonding process, the second aperture array is vapor deposited on the glass wafer. In general, up to 148 individual MEMS chips with sizes of 6 mm $\times$ 6 mm can be manufactured on one wafer. During the dicing of the chips, water has to applied to the current cutting location to remove the debris and the generated heat.

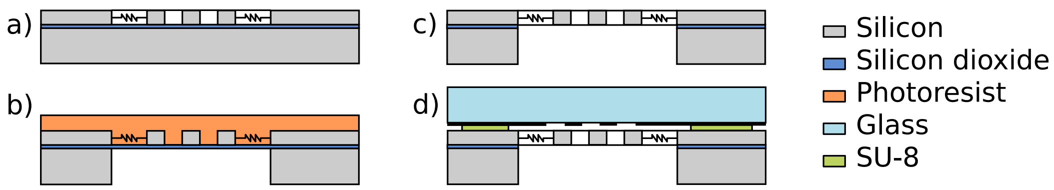

Figure 1.5: Diagram of the fabrication steps: a) Plasma etching of the device layer. b) Photoresist covering of the microstructures for protection and subsequent backside etch. c) Wet etching of SiO_2 and release of the movable microstructure. d) Bonding of the glass-wafer with the vapor deposited metal aperture using SU-8 as bonding adhesive [1].

1.4 Problems of First MEMS Generation and Countermeasures

The fabrication of the first MEMS generation has revealed that water of the cutting process has partly reached the interior of the MEMS microstructures via channels which

electrically separate the MEMS parts. This water transports debris into the gaps of the microstructures and impairs their movement and with it the electro-mechanical transduction. In general, there are two ways to address this issue: by adapting the fabrication process or by changing the chip design.
Some additional fabrication steps have been considered and/or tested: One possible method to remove the water from the microstructures is to dry the chip after dicing. Nevertheless, capillary forces during the drying process decrease the distance between the movable microstructure and glass and, hence, increase the probability that the microstructure sticks to the glass blocking the electro-mechanical transduction. To minimize the capillary forces, super-critical drying could be considered. Another possibility is to rinse the chip with isopropanol which also removes the water from the movable microstructure. Although the rinsing of the chip with isopropanol was successfully tested, this step proved to be very challenging. Therefore, it is not really a feasible fabrication step. LASER cutting is a method which does not require any water rinsing but such an additional fabrication step would significantly increase the production costs and is not available at the Institue of Sensor and Actuator Systems.
Many options are given to design the electro-mechanical transducer and, therefore, the water problem could be circumvented by redesign. On the one hand, meander-shaped microchannels could be introduced to increase the fluidic resistance. On the other hand, a blocking element in the microchannels can prevent the water from penetrating the chip but it has to be removed after dicing. Otherwise, the inner part of the sensor would be electrically shielded from the outside.
The expectable electrostatic forces on the MEMS transducers are generally very small resulting in small displacements and low sensitivities. The MEMS transducer of the first generation exhibited only small sensitivities to electric fields of, e.g., 1 kV/cm, while otherwise, e.g., acoustically induced vibrations have a large influence on the output signal. Redesigning the transducer can significantly increase its sensitivity to electric fields and minimize noise stemming from these vibrations.

1.5 Aim of Diploma Thesis

The aims are:

- Development of a Finite-Element simulation model in COMSOL Multiphyics for electric field sensors.
- Optimization of the chip design based on Finite-Element simulations.
- Implementation of the new chip designs into the existing Python-code for generating the lithograhy masks.
- Investigation of the new chip generation after fabrication.

2 Introduction to Simulations of Electric Field Sensing

2.1 Introduction to COMSOL Multiphysics

This section is partly based on the *COMSOL Multiphysics User's Guide* [19]. COMSOL Multiphysics ® is an environment for modeling and solving various kinds of scientific and engineering problems which allows the extension from conventional models for one type of physics into multiphysics models to solve coupled phenomena. Within the scope of this thesis, the version COMSOL 5.1. is used. In this section, only an extreme concise review of COMSOL Multiphysics can be given, focussing on features which are important for simulations of the electric field microsensor.

The model and its components can be defined in the so-called Model Builder, where a model tree is built [20]. A new model is created by starting with the default model tree. In this case, all of the nodes are the so-called top-level parent nodes and by right-clicking them, child nodes or subnodes are shown and can be added to the tree. By right-clicking the child nodes, their node settings can be edited. A simple model tree is illustrated in Fig. 2.1.

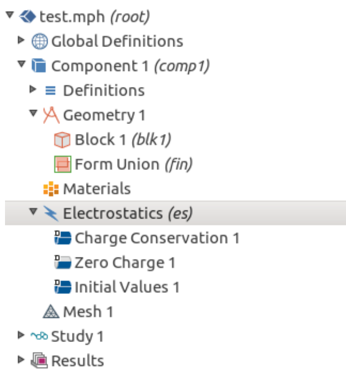

Figure 2.1: A picture of a simple model tree. The top-level parent nodes *Global Definitions*, *Component 1*, *Study 1* and *Results* are subnodes of the root node *test.mph* and have, themselves, subnodes. For example, *Definitions* is a subnode of *Component 1*.

In general, a model tree has a root node which is the name of the multiphysics model file (or MPH file) where this model is saved to. The first subnodes, also called the top-level parent nodes, of the root node are:

- *Global Definitions*
- *Component*
- *Study*
- *Results*

The nodes *Global Definitions* and *Results* are created by default and the two additional top-level node types *Component* and *Study* are usually built by the Model Wizard which appears after starting COMSOL. They can also be generated by right-clicking the root node and selecting *Add Component* and *Add Study*.

2.1.1 Global Definitions Node

In *Global Defintions* parameters, variables and functions, which can be used throughout the model, can be defined. Within the scope of this diploma thesis, the subnode *Parameters* has been used. In general, parameters are user-defined constant scalars, which are especially important for parameterizing geometric dimensions, specifying mesh element sizes or defining parametric sweeps [21]. Parametric sweeps are simulations that are repeated for a variety of different values of parameters such as the size of a sphere or the distance between two bodies. A parameter expression can contain numbers, other parameters, built-in constants, built-in functions and unary and binary operators. One has to consider that some names are already reserved for built-in constants. Some important examples are:

- Mathematical constants like π (3.1415...) and the imaginary unit i.
- Mathematical functions like cos, sin, tan, exp, or sqrt.
- Physical constants like *g_const* (acceleration of gravity), *c_const* (speed of light), or *R_const* (universal gas constant).
- The time variable t.

2.1.2 Component Node

The top-level parent node *Component* has the following subnodes:

- *Definitions*
- *Geometry*
- *Materials*
- *Mesh*

The types of physics, which can be selected in the Model Wizard or by right-clicking *Component*, are also added to these subnodes.

For simulations of the electric field microsensor, the physics *Electrostatics*, *Electric Currents* and *Electric Currents/Shell* are of interest.

In *Definitions*, local definitions, which are only applied to this specific model, i.e. this specific component, can be added. Within the frame of this thesis, the *Definition*'s child node *Selections* has been used: Here, a set of geometric entities for reuse throughout the model can be created by the user.

By right-clicking *Geometry*, different geometries, such as boxes or spheres, can be selected and added to the model. While boxes and spheres are examples for directly generated 3D objects, it is also possible to generate 3D geometries based on 2D sections which can be created in the so-called *Work Plane*. A *Work Plane* is a 2D plane, whose orientation in the 3D space is defined in the settings of *Work Plane*. The 2D structure can then be converted into 3D by extrusion or revolving. Furthermore, it is possible to edit existing geometries: In *Geometry*'s child node *Booleans and Partitions* objects can be united or subtracted from each other, in *Transforms* 3D geometries can be copied, moved, mirrored, rotated or scaled.

By right-clicking the *Materials* node, materials with their particular properties can be selected out of a material library and added to the model. For the electric field microsensor, the materials air, silicon and chromium are of interest and for the physics *Electrostatics*, *Electric Currents* and *Electric Current, Shell* the material properties relative permittivity ε_r and electrical conductivity σ_el are required. The assignment of properties to geometries is similar for material, physics and meshing properties: In general, a specific property, like the material type air, can be assigned to a certain geometric entity, like a box, via the Geometric Entity Selection. Here, the geometric entity level is either Domain (3D), Boundary (2D), Edge (1D) or Point (0D). The final selection is done either by selecting geometric entities, which have already been defined in *Definitions*, or manually by clicking the geometric entities in the Graphics window, where they are visualized.

In general, when solving the problems, COMSOL Multiphysics uses the finite element method (FEM). For this, the domains need to be discretized, in the case of 3D geometries into tetrahedral, hexahedral, prism or pyramid mesh elements [22]. The boundaries in the geometries are discretized into triangular or quadrilateral boundary elements, while the edges are subdivided into edge elements. The discretization is carried out by the mesh generator and the meshing properties can be set in *Mesh*. The default is to use a mesh that is adapted to the current physics settings in the model. This can be set in the mesh setting by selecting the physics-controlled mesh as the sequence type. By selecting the user-controlled mesh as the sequence type, it is possible to manually build and edit the meshing sequence using various meshing techniques. For the 3D simulation of the electric field microsensor in an external electric field, the 3D *Free Tetrahedral* mesh and the 2D *Free Triangular* mesh have been applied within the scope of this diploma thesis. In general, the mesh element sizes range from extremely fine to extremely coarse and are selected according to the dimensions of the problem and to the desired precision of the simulation. If, for example, the geometry consists of two spatially separated boxes and one of them is much smaller than the other one, the smaller box needs a finer mesh than the larger box. Individual parameters, such as the maximum and minimum element size or the maximum element growth rate, can also be customized.

2.1.3 Study Node

The process of solving a problem in COMSOL is divided into a hierarchy of different details [23]. On the coarsest level, containing the least amount of detail, is the *Study* node. By right-clicking the root node or by using the Model Wizard after creating a new MPH-file, any of the following predefined Study types can be added to the model tree:

- *Eigenfrequency*
- *Frequency Domain*
- *Small-Signal Analysis, Frequency Domain*
- *Stationary*
- *Time Dependent*

The electric field microsensor should measure static or slowly changing electric fields. Hence, the study type *Stationary* is used to generate equations without time derivatives.

By selecting one of the predefined study types, a corresponding study step is automatically added as a subnode to *Study*. For the stationary study type, this subnode is called *Step 1: Stationary*. The study step represents the next level of detail and controls the form of equations, which physical interfaces and which meshes are applied. The solver sequence corresponding to the study step is the next level of detail and is added as a further subnode to *Study* with the description *Solver Configurations*. A solver sequence contains nodes that define variables to solve for (*Dependent Variables*), the solvers (in the case of the stationary study type *Stationary Solver*), their settings and additional sequence nodes for storing the solution. For the physics *Electrostatics*, *Electric Currents* and *Electric Currents/Shell*, the dependent variable of each physics type, which is also the variable to solve for, is the electric potential.

Solving the problem is finally done by right-clicking *Study* and selecting *Compute*, which generates a default solver sequence for the corresponding study steps and computes the solution. There are some study steps which do not generate equations and can only be used in combination with other study steps. One of these additional study steps, which has been selected, is *Parametric Sweep*: This is used to formulate a sequence of problems by varying some parameters which are defined in *Global Definitions*. In the settings of the *Study*'s subnode *Parametric Sweep*, the parameter value range is set. If more than one parameter is varied, the desired parameter combinations can also be specified.

2.1.4 Results node

The *Results* node has the following subnodes:

- *Data Sets*
- *Derived Values*
- *Tables*
- *Export*
- *Reports*

Data Sets contains the solutions of the computation and different studies are stored in different data sets. For example, the data set for a parametric sweep is indicated by *Study 1/Parametric Solutions 1*, while the data set for a study without variations of any parameters is called *Study 1/Solution 1*.

In *Derived Values*, one can access values of a specific data set and either display them or use them for further calculations. For example, in the physics type *Electrostatics* the electromagnetic force acting on a certain domain can be calculated. This value can then be accessed via *Derived Values*. For the optimization of the electric field microsensor design, the electromagnetic forces acting on the sensing elements need to be maximized and, hence, are of special interest. As the calculated electromagnetic force already represents the force acting on an entire domain, no further calculations are necessary and it is sufficient to only evaluate the calculated force. For this, the *Derived Value*'s subnode *Global evaluation* has been used within the scope of this diploma thesis, while other subnodes like *Average* or *Integration* have not been applied.

In *Tables*, the derived values are displayed.

In *Export*, data and tables can be exported as txt-files, which has been used within the scope of this diploma thesis for data analysis of parametric sweeps. Images can also be exported.

Additionally to the *Results*' subnodes, there is also a child node for visualizing the dependent variables of the physics types which have been added to the model. For the physics types *Electrostatics*, *Electric Currents* and *Electric Currents, Shell* the dependent value is the electric potential. This scalar field can be visualized in many ways, such as in volume, surface or multislice plots.

2.2 Physics for Simulations of Electric Field Microsensors

2.2.1 Basics of Electrostatics

This chapter is a theoretical summary of the most important principles of electrostatics, which are required not only for COMSOL simulations but also for the basic understanding of the electric field sensing concept. The content of this chapter roughly follows the book "Electromagnetism" by G. L. Pollack and D. R. Stump [24].

Electric Field and Electric Potential

Electrostatics is the science of interactions between electric charges and the electric field in static systems [25]. The charges must be at rest and the fields constant over time. Practically, so-called quasi-static systems, which slowly change in time, can also be described with electrostatics using the quasi-static approximation. All of electrostatics can be derived from two principles: Coulomb's law and the superposition principle. The empiric Coulomb's law describes the force $\mathbf{F}_1$ acting on a point-like charge q_1 at a position $\mathbf{x}_1$ due to the presence of another point-like charge q_2 at a position $\mathbf{x}_2$ and is given by the equation

$$\mathbf{F}_1 = \frac{1}{4\pi\varepsilon_0}\frac{q_1 q_2(\mathbf{x}_1 - \mathbf{x}_2)}{|\mathbf{x}_1 - \mathbf{x}_2|^3}, \tag{2.1}$$

where ε_0 is the permittivity of vacuum. The superposition principle states that the force on a charge q at a position $\mathbf{x}$ due to a set of charges $\{\ q_1, q_2, q_3, ..., q_N\ \}$ at the positions $\{\ \mathbf{x}_1, \mathbf{x}_2, \mathbf{x}_3, ..., \mathbf{x}_N\ \}$ is the sum of the individual Coulomb forces:

$$\mathbf{F}_\mathrm{q} = \frac{1}{4\pi\varepsilon_0}\sum_{i=1}^{N}\frac{q q_i(\mathbf{x} - \mathbf{x}_i)}{|\mathbf{x} - \mathbf{x}_i|^3}. \tag{2.2}$$

The main quantity for describing electrostatic problems is the electric field which is a vector field. The definition of the electric field $\mathbf{E}(\mathbf{x})$ is the force per unit charge, which would act on a small test charge q in the limit $q \to 0$ if it would be located at $\mathbf{x}$:

$$\mathbf{E}(\mathbf{x}) = \lim_{q\to 0}\frac{\mathbf{F}}{q}. \tag{2.3}$$

The test charge is chosen to be small so that it does not influence the other charges. The electric field is a measure for the force distribution as the force acting on a charged particle q at the position $\mathbf{x}$ in a given electric field $\mathbf{E}$ can be calculated by

$$\mathbf{F} = q\mathbf{E}(\mathbf{x}). \tag{2.4}$$

Any field can be distributed in discrete point-like sources, as in Eq. (2.2), because charges are located in elementary particles like electrons or protons. However, these microscopic charges are much smaller than the length scales of any macroscopic system. Therefore, in a macroscopic system, it is a good approximation to replace the discrete distribution of charges by a continuous distribution of charges, given by the volume charge density $\rho(\mathbf{x})$. As a consequence of this continuum approach, the sum in Eq. (2.2) is replaced by an integral over the volume of the continuous charge distribution:

$$\mathbf{E}(\mathbf{x}) = \frac{1}{4\pi\varepsilon_0}\int\frac{\rho(\mathbf{x})(\mathbf{x} - \mathbf{x}')}{|\mathbf{x} - \mathbf{x}'|^3}\mathrm{d}^3x', \tag{2.5}$$

where $\mathrm{d}x'$ is the integration variable. For instance, d^3x' becomes $\mathrm{d}x\mathrm{d}y\mathrm{d}z$ for the integration in the Cartesian coordinate system. Eq. (2.5) is fundamental in electrostatics because the electric field can be calculated just by knowing the charge density throughout the source. However, the integration in the three space coordinates becomes more challenging if the charge configuration is more complex. By transforming Eq. (2.5) into Eq. (2.6), the existence of a scalar field called the electric potential $V(\mathbf{x})$ can be postulated:

$$\mathbf{E}(\mathbf{x}) = -\nabla[\frac{1}{4\pi\varepsilon_0}\int\frac{\rho(\mathbf{x})}{|\mathbf{x}-\mathbf{x}'|}\mathrm{d}^3x'] = -\nabla V(\mathbf{x}). \tag{2.6}$$

For every electrostatic problem which includes conductors and dielectrics in the system, the solution for the electric field is unique. As the electric potential can be calculated by integrating the electric field, an integration constant is generated so that the electric potential is determined only up to this additive constant. Therefore, a reference point, where the electric potential has a certain value, can be arbitrarily chosen. If the total charge in a system is finite, the reference point is usually chosen to be at infinity, where the electric potential is assumed to be 0. In general, the electric potential $V(\mathbf{x})$ is a measure for the work W_γ, which is necessary for transporting a charge from a start position $\mathbf{x}_1$ to an end position $\mathbf{x}_2$ along a trajectory γ, according to

$$W_\gamma = \int_\gamma \mathbf{F}\mathrm{d}\mathbf{x} = q\int_\gamma \mathbf{E}(\mathbf{x})\mathrm{d}\mathbf{x} = q\int_\gamma -\nabla V(\mathbf{x})\mathrm{d}\mathbf{x} = -q[V(\mathbf{x}_2) - V(\mathbf{x}_1)]. \tag{2.7}$$

If the reference point is assumed to be at infinity, the electric potential at a position $\mathbf{x}$ is the work, which is necessary for bringing a unit charge from infinity to its final position $\mathbf{x}$. As the electric field can be described as the gradient of a scalar field, it is irrotational, which is decribed in the first Maxwell equation of electrostatics in Eq. (2.8). The second Maxell-equation of electrostatics is also called Gauss's law and is formulated in Eq. (2.9).

$$\nabla \times \mathbf{E}(\mathbf{x}) = \mathbf{0}, \tag{2.8}$$

$$\nabla \cdot \mathbf{E}(\mathbf{x}) = \frac{\rho(\mathbf{x})}{\varepsilon_0}. \tag{2.9}$$

As a result of Eq. (2.8), the line integral and, thus, the work for bringing a charge of the electric field from one point to another is independent of the pathway. As a consequence of Eq. (2.9), the electric field is a divergence field, which means that each electric field line has an origin and an end point. In the case of two spatially separated charges with q and $-q$, the electric field lines start at the positive charge, head in the direction of and end at the negative charge. By combining the two Maxwell equations of electrostatics, one can obtain the Poisson's equation

$$\Delta V(\mathbf{x}) = \frac{\rho(\mathbf{x})}{\varepsilon_0}. \tag{2.10}$$

If the space where the electric potential should be determined is free of charge, the equation reduces to $\Delta V = 0$ (Laplace's equation). By solving the second-order differential equation, together with the boundary conditions, the electric potential and, hence, the electric field can be calculated.

Electrostatics and Conductors

In a conductor some of the electrons are free to move macroscopic distances. This movement is characterized by the electrical conductivity [26]. On the microscopic scale, these electrons are in the periodic potential of a lattice of positive metallic ions making only small oscillations around their equilibrium position. Without an electric field, the free electrons are uniformly distributed within the conductor. However, if an electric field is applied, the free electrons will move in response to the electric force $\mathbf{F} = -e\mathbf{E}$ until a new equilibrium is reached. This happens when $\mathbf{E} = 0$ inside the conductor. In a typical metal, the conductivity is large so that this electrostatic equilibrium is reached in a very short period of time. All calculations in electrostatics assume that the system is in this equilibrium, where the charges do not move anymore. As the electrons will accumulate somewhere on the conductor's surface to cancel out the inner electric field, the surface charge density plays an important role. It can be calculated by considering the following continuity conditions of the electric field in electrostatics:

$$\mathbf{E}_1^{||} = \mathbf{E}_2^{||} \; \forall \, \mathbf{x} \in S \tag{2.11}$$

$$\text{and} \;\; \mathbf{E}_1^{\perp} - \mathbf{E}_2^{\perp} = \frac{\sigma(\mathbf{x})}{\varepsilon_0} \; \forall \, \mathbf{x} \in S, \tag{2.12}$$

where $\mathbf{E}_1$ and $\mathbf{E}_2$ are the electric field components in the volumes V_1 and V_2, which are separated by the interface S. Eq. (2.11) states that the component of the electric field which is parallel to the boundary surface does not change at the interface S. As a result of Eq. (2.12), the E-field component which is perpendicular to the boundary surface does change at the interface S. The step in $\mathbf{E}^{\perp}$ at S depends on the surface charge density in S.

The conductor is confined to a 3D object with volume V and surface ∂V and its properties in the equilibrium state in a static E-field can be summarized by:

- $\mathbf{E}(\mathbf{x}) = 0 \; \forall \, \mathbf{x} \in V$,
- $\rho(\mathbf{x}) = 0 \; \forall \, \mathbf{x} \in V$,
- $V(\mathbf{x}) = V_0 = \text{const.} \; \forall \, \mathbf{x} \in V \cup \partial V$,
- $\sigma(\mathbf{x}) = \varepsilon_0 \cdot \mathbf{E}_{\text{outer}}^{\perp}(\mathbf{x}) \; \forall \, \mathbf{x} \in \partial V$ where $\mathbf{E}_{\text{outer}}$ is the electric field outside of the conductor.

When an electric field is applied to a conductor, the electromagnetic forces act only on the conductor's surface where the charges are accumulated in the electrostatic equilibrium. The force on a small area A of the surface is $\mathbf{F} = q\mathbf{E}^{\perp} = \sigma A \mathbf{E}^{\perp}$, with $\mathbf{E}^{\perp}$ being discontinuous at the surface. It is 0 inside and σ/ε_0 outside and so it is not obvious which value should be taken. In general, the external field $\mathbf{E}^{\perp}$ is generated by the local surface charges in the immediate area and by all the other charges on the conductor. In calculating the force on the local surface charges in a small area, their own contribution to the field should not be included. As near the surface the local charge density appears as an infinite plane of charge, the contribution from local charges can be calculated and is then given by $\mathbf{E}^{\perp}(\text{local}) = \sigma/2\varepsilon_0$. The contribution from the other charges must be $\mathbf{E}(\text{non} - \text{local}) = \sigma/2\varepsilon_0$ so that the final outward force on the surface of a conductor is given by

$$\mathbf{F}(\mathbf{x}) = q\mathbf{E}^{\perp}(\mathbf{x}) = \sigma A \mathbf{E}^{\perp}_{\text{non-local}}(\mathbf{x}) = A\frac{\sigma^2}{2\varepsilon_0}\hat{\mathbf{n}}, \tag{2.13}$$

where $\hat{\mathbf{n}}$ is the unit vector perpendicular to a small area A of the conductor.

Solving Laplace's Equation

In general, the field outside the conductor is different from the original field because it includes Coulomb-field contributions of the displaced conduction electrons. One property of a conductor in equilibrium with static fields is the constant electric potential on its surface. If the electric potential outside of the conductor should be determined by solving Poisson's equation (2.10), this equipotential surface generates the boundary conditions for the second-order differential equation. In order to illustrate the procedure to solve the Laplace's equation with boundary conditions, consider two plane conducting plates separated by a vacuum gap with the width d, wherein the electric potential should be calculated [27]. This parallel plate capacitor is illustrated in Fig. 2.2.

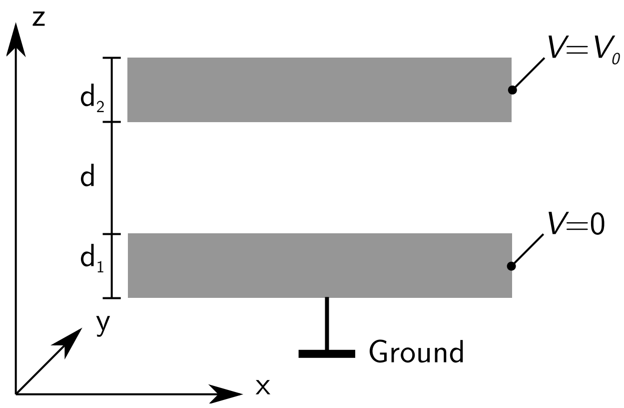

Figure 2.2: Parallel plate capacitor: The conductor at $z = 0$ is grounded so that $V = 0$, while the conducting plate at $z = d$ is kept at potential V_0. It is assumed that the plates are expanded to infinity in the x- and y-direction.

Let us assume that the plate dimensions are much larger than the gap, a translation invariance in directions parallel to the plates is generated. If the conducting plates are located parallel to the xy-plane, this symmetry makes all quantities independent of x and y. The problem is reduced to the following equation and boundary conditions:

$$\Delta V(\mathbf{x}) = 0 \leftrightarrow \frac{\mathrm{d}^2 V}{\mathrm{d}z^2} = 0 \; \forall \, \mathbf{x} \text{ with } z \in [0, d] \tag{2.14}$$

$$V(z=0) = 0 \text{ and } V(z=d) = V_0. \tag{2.15}$$

The solution of Laplace's equation is $V(z) = V_0 z/d$ and the corresponding field, obtained from $\mathbf{E} = -\nabla V$, is $E_\mathrm{z}(z) = -V_0/d$. This is an example for solving Laplace's equation in Cartesian coordinates.

In general, it is valuable to find symmetries in the given electrostatic problem, otherwise the solution of the second-order differential equation can become very challenging. In problems with cylindrical or spherical symmetry, it is more convenient to choose appropriate curvilinear coordinates over Cartesian coordinates. For this, the formulas for calculating the gradient, divergence or Laplacian operator need to be modified [28]. In general terms, let u_1, u_2, u_3 denote three coordinates which specify the points in three dimensions. For example, the Cartesian coordinates are represented by $u_1 = x$, $u_2 = y$ and $u_3 = z$, while the spherical coordinates are $u_1 = r$, $u_2 = \theta$ and $u_3 = \phi$. The corresponding unit vectors $\hat{\mathbf{e}}_1$, $\hat{\mathbf{e}}_2$, $\hat{\mathbf{e}}_3$ point in the directions of independent positive displacements of u_1, u_2, u_3, respectively. In the case of a spherical coordinate system, the unit vectors are $\hat{\mathbf{e}}_\mathrm{r}$, $\hat{\mathbf{e}}_\phi$ and $\hat{\mathbf{e}}_\theta$. The unit vectors are assumed to be orthogonal at each point in space. The infinitesimal displacement $\mathrm{d}\mathbf{s}$ in space, which results from changing the coordinates by $\mathrm{d}u_1$, $\mathrm{d}u_2$, $\mathrm{d}u_3$, is given by

$$\mathrm{d}\mathbf{s} = \hat{\mathbf{e}}_1 h_1 \mathrm{d}u_1 + \hat{\mathbf{e}}_2 h_2 \mathrm{d}u_2 + \hat{\mathbf{e}}_3 h_3 \mathrm{d}u_3. \tag{2.16}$$

In this case, h_1, h_2 and h_3 are scale factors related to the distances $\mathrm{d}s_i$ to change of coordinate $\mathrm{d}u_i$. In the case of spherical coordinates, the displacement out of a position $\mathbf{x} = r\hat{\mathbf{e}}_\mathrm{r}$ is $\mathrm{d}\mathbf{s} = \hat{\mathbf{e}}_\mathrm{r}\mathrm{d}r + \hat{\mathbf{e}}_\theta r\mathrm{d}\theta + \hat{\mathbf{e}}_\phi r\sin\theta\mathrm{d}\phi$. So the scale factors for the spherical coordinate system are: $h_\mathrm{r} = 1$, $h_\phi = r\sin\theta$ and $h_\theta = r$. In order to transform the Poisson's equation or Laplace's equation into a spherical coordinate system, the Cartesian Laplacian $\Delta = \frac{\partial^2}{\partial x^2} + \frac{\partial^2}{\partial y^2} + \frac{\partial^2}{\partial z^2}$ needs to be transformed. The Laplacian operator in an arbitrary coordinate system with the scale factors h_i, where $i = 1, 2, 3$ is given by

$$\Delta f = \partial_i(\partial_i f) = \frac{1}{h_1 h_2 h_3}\partial_\alpha\left(\frac{h_1 h_2 h_3}{h_\alpha^2}\partial_\alpha f\right). \tag{2.17}$$

Eq. (2.17) is written in the so-called index or suffix notation [29]: Here, the dot-product, for example, is given by: $\mathbf{A}\cdot\mathbf{B} = A_\mathrm{x}B_\mathrm{x} + A_\mathrm{y}B_\mathrm{y} + A_\mathrm{z}B_\mathrm{z} = A_i B_i$. The suffix notation makes use of the Einstein summation convention: Any repeated suffix is understood to be summed from 1 to 3, so that $A_i B_i$ means $\sum_{i=1}^{3} A_i B_i$. A derivative is given by: $\frac{\partial f}{\partial x} = \partial_\mathrm{x} f$. By inserting the corresponding scale factors in Eq. (2.17), the Laplacian operator of the spherical coordinate system becomes:

$$\Delta f = \frac{1}{r^2}\partial_\mathrm{r}(r^2\partial_\mathrm{r} f) + \frac{1}{r^2\sin\theta}\partial_\theta(\sin\theta\partial_\theta f) + \frac{1}{r^2\sin\theta^2}\partial_\phi\partial_\phi f. \tag{2.18}$$

A conducting sphere of radius a carrying a charge Q_0 represents a simle electrostatic problem with spherical symmetry [30]. Due to the radial symmetry of this geometry, the problem does not depend on the polar coordinate θ or the azimuthal coordinate ϕ. Laplace's equation and the boundary conditions of this problem are

$$\frac{1}{r^2}\frac{\mathrm{d}}{\mathrm{d}r}\left(r^2\frac{\mathrm{d}V}{\mathrm{d}r}\right) = 0, \tag{2.19}$$

$$V(a) = V_0 \text{ and } \lim_{r\to\infty} V(r) = 0. \tag{2.20}$$

The general solution of this second-order differential equation for $r \in [a, \infty)$ is

$$V(r) = \frac{A}{r} + B, \tag{2.21}$$

where A and B are constants determined by the boundary conditions in Eq. (2.20). The condition $V(\infty) = 0$ and $V(a) = V_0$ require $B = 0$ and $A = V_0 a$, respectively. Thus, the electric potential for $r \in [a, \infty)$ in the presence of a conducting sphere with radius a and charge Q_0 becomes

$$V(r) = \frac{V_0 a}{r}. \tag{2.22}$$

The electric field is: $E^i(x^m) = -\partial_i V = -\partial_\mathrm{r} V = -\frac{V_0 a}{r^2} e^i_\mathrm{r}$, where e^i_r is the unit vector pointing in the radial direction.

Electrostatics and Dielectrics

In a metal some electrons are free to move throughout the conductor. In an insulator (also called dielectric) the electrons are bound to their atoms or molecules via Coulomb forces and, hence, cannot move [31]. When an external electric field is applied to a dielectric, electrons and nuclei become displaced by small distances, the positively charged nuclei in the direction of $\mathbf{E}$ and the negatively charged electrons in the opposite direction. This mechanism, where electric dipoles are induced in the atoms, is called induced polarization. An electric dipole is composed of two equal but opposite charges $q_1 = q$ and $q_2 = -q$ with a distance $d \to 0$. The electric dipole moment is defined by $\mathbf{p} = q\mathbf{d}$ [32]. If permanent electric dipoles are present, they are aligned parallel to an external E-field. This so-called orientation polarization superimposes the induced polarization. If ions reside in the dielectric, they are also moved in response to an outer field. In this case, it is assumed that no ions and polar molecules reside in the dielectric. In equilibrium, a single atom in an electric field $\mathbf{E}$ has a dipole moment proportional to the field $\mathbf{p} = q\mathbf{d} = \alpha\mathbf{E}$, where q is the value of the positive charge of the nucleus and the absolute value of the negative charge of the electrons. The distance vector between the positive and negative charge concentration is given by $\mathbf{d}$, and α is the so-called atomic polarizability which has to be determined by experiment for individual atoms. In order to account for effects of atomic polarizability, it is necessary to define the dielectric polarization $\mathbf{P}(\mathbf{x})$ which is the mean dipole moment density of a dielectric. The polarization at a position $\mathbf{x}$ is the sum of dipole moments in the dielectric per unit volume:

$$\mathbf{P}(\mathbf{x}) = \frac{1}{\delta V}\sum_{i=1}^{\delta N}\mathbf{p}_i. \tag{2.23}$$

In Eq. (2.23) $\mathbf{p}_i$ denotes the dipole moment of the atom i in the volume δV and δN the number of atoms in δV. Due to the high number of atoms even in small volumes δV, the dielectric polarization $\mathbf{P}(\mathbf{x})$ is a smooth function of $\mathbf{x}$.

The mean charge density resulting from polarization in an external electric field is called the bound charge density $\rho_\mathrm{B}(\mathbf{x})$. For the relationship between ρ_B and $\mathbf{P}$, an arbitrary volume V entirely inside the dielectric can be considered. When the dielectric is not polarized, the total charge inside V is zero. In response to an external electric field, the material becomes polarized and the net charge Q_across will move across the surface $S = \partial V$ of V because atoms near S become distorted. Considering charge conservation, the net charge in V after complete polarization of the dielectric is $-Q_\mathrm{across}$, so that

$$\int_V \rho_\mathrm{B}\mathrm{d}^3x = -Q_\mathrm{across}. \tag{2.24}$$

The net charge $Q_\mathrm{across} = \int_S \sigma_\mathrm{B}\mathrm{d}A = \int_{S=\partial V}\mathbf{P}\cdot\mathrm{d}\mathbf{A}$ can be converted into $Q_\mathrm{across} = \int_V \mathrm{div}\mathbf{P}\mathrm{d}V$ by applying the Gauss's theorem [33]. Here, σ_B is the bound charge density in $S = \partial V$. By inserting Q_across into Eq. (2.24), the relationship between the bound charge density and the polarization becomes

$$\mathrm{div}(\mathbf{P}) = -\rho_\mathrm{B}(\mathbf{x}). \tag{2.25}$$

If the polarization field is uniform, i.e. independent of $\mathbf{x}$, then $\rho_\mathrm{B}(\mathbf{x})$ is 0. In this case, the bound charges lie only on the surface of the dielectric, with the density $\sigma_\mathrm{B} = \hat{\mathbf{n}}\cdot\mathbf{P}$. If the polarization varies within the dielectric, there is a nonzero bound charge at points where $\mathbf{P}(\mathbf{x})$ diverges, with density $-\mathrm{div}(\mathbf{P}(\mathbf{x}))$.

The fundamental equations for the static electric field are given by the two Maxwell equations of electrostatics (2.8) and (2.9). These equations are valid both in vacuum and dielectrics, because, in either case, ρ must include all the charge sources. While only free charge sources are of interest in the case of a perfect conductor, the charge density of a dielectric needs to be separated into bound charge $\rho_\mathrm{B}(\mathbf{x})$ and free charge $\rho_\mathrm{F}(\mathbf{x})$ which is the charge placed in the system from the outside. The total charge density is equal to $\varepsilon_0\nabla\cdot\mathbf{E}$, according to the second Maxwell equation (2.9), and the bound charge density is $-\nabla\cdot\mathbf{P}$ due to Eq. (2.25) so that the free charge density becomes

$$\rho_\mathrm{F}(\mathbf{x}) = \rho(\mathbf{x}) - \rho_\mathrm{B}(\mathbf{x}) = \nabla\cdot(\varepsilon_0\mathbf{E} + \mathbf{P}). \tag{2.26}$$

The sum $\varepsilon_0\mathbf{E}+\mathbf{P}$ is the so-called displacement field $\mathbf{D}(\mathbf{x})$. With the electric displacement field, equation (2.26) becomes

$$\nabla\cdot\mathbf{D} = \rho_\mathrm{F}. \tag{2.27}$$

An insulating material, for which $\mathbf{P}(\mathbf{x})$ is proportional to $\mathbf{E}(\mathbf{x})$, is called an isotropic linear dielectric. Dilute gases, liquids and amorphous solids such as glass and plastics are examples of linear dielectrics. In this case, only one parameter is needed to relate $\mathbf{P}$ and $\mathbf{E}$. However, three constants are conventionally used: the susceptibility χ_e, the permittivity ε and the dielectric constant κ. Any one of these parameters determines the other two. The electric susceptibility is used to relate the electric field with the polarization $\mathbf{P} = \varepsilon_0\chi_\mathrm{e}\mathbf{E}$. The greater the electric susceptibility, the greater the ability of a material to polarize in response to the field. The permittivity of a material relates the dielectric displacement field with the applied electric field by $\mathbf{D} = \varepsilon_0\mathbf{E}+\mathbf{P} = \varepsilon_0(1+\chi_\mathrm{e})\mathbf{E} = \varepsilon\mathbf{E}$, where the permittivity is determined by the susceptibility via $\varepsilon = \varepsilon_0(1+\chi_\mathrm{e})$. The dielectric constant κ is defined by $\kappa = 1+\chi_\mathrm{e}$ and is also called relative permittivity.

As opposed to isotropic materials, solid crystals generally behave differently since $\mathbf{P}$ may have nonzero components perpendicular to $\mathbf{E}$. Therefore, the three constants χ_e, ε and κ become tensors instead of scalars. $\mathbf{D} = \varepsilon\mathbf{E}$ is one of the so-called constitutive relations which describe the macroscopic properties of the medium.
The boundary conditions for dielectrics are [34]:

$$\mathbf{E}_1^{||} = \mathbf{E}_2^{||} \;\forall\, \mathbf{x} \in S \tag{2.28}$$

$$\text{and}\;\; \mathbf{D}_1^{\perp} - \mathbf{D}_2^{\perp} = \sigma_\mathrm{F}(\mathbf{x}) \;\forall\, \mathbf{x} \in S, \tag{2.29}$$

where $\mathbf{E}_1$ and $\mathbf{E}_2$ are the electric fields and $\mathbf{D}_1$ and $\mathbf{D}_2$ are the displacement fields in the volumes V_1 and V_2 (with different permittivities ε_1 and ε_2) , which are separated by a surface S. Furthermore, σ_F is the free charge density in S. As a result of Eq. (2.28), the component of the electric field parallel to the boundary surface does not change at the interface S, which is also the case in electrostatic problems without dielectrics. Equation (2.29) states that the component of the displacement field perpendicular to S changes at the interface to an extent which depends on the free charge density in the boundary surface.

2.2.2 Electrostatics Interface in COMSOL

The *Electrostatics* interface comprises the equations, boundary conditions and space charges for modeling electrostatic fields, solving for the electric potential $V(\mathbf{x})$ which is, hence, the dependent variable of this physics type [35].

Equations to be solved

The equations, which are solved in the *Electrostatics* interface, are

$$\mathbf{E} = -\nabla V \tag{2.30}$$

$$\text{and}\quad -\nabla(\varepsilon_0\nabla V - \mathbf{P}) = \rho_\mathrm{F}. \tag{2.31}$$

The second equation has been derived in subsection 2.2.1 and represents a second-order differential equation which is similar to Poisson's equation. As a result of Eq. (2.31), it is obviously assumed that the electric potential is determined in dielectric materials and, hence, the permittivity ε of each material, which is added to the study, has to be given. In general, the permittivity is the measure of resistance which is encountered when forming an electric field in a medium and has been described in detail in subsection 2.2.1. More precisely, the relative permittivity $\varepsilon_{\mathrm{r}} = \kappa$, which is the ratio between the permittivity of the material and the permittivity of vacuum ($\varepsilon(\text{vacuum}) = \varepsilon_0$), needs to be inserted for each material in COMSOL. If the material is a metal like copper, the relative permittivity can be set to 1. While the relative permittivity of air is also approximately 1, it is, in general, greater than 1, e.g. 11 in the case of silicon.

Boundary conditions

The relevant condition at interfaces between different media, which has been introduced in subsection 2.2.1, is given by

$$\mathbf{n}_2 \cdot (\mathbf{D}_1 - \mathbf{D}_2) = \sigma_{\mathrm{F}}(\mathbf{x}) \ \forall \ \mathbf{x} \in S, \tag{2.32}$$

where $\mathbf{D}_1$ and $\mathbf{D}_2$ are the displacement fields in the volumes Ω_1 (with ε_1) and Ω_2 (with ε_2) which are separated by the interface S. σ_{F} is the free charge density in this interface.

Further boundary conditions, which have been used within the scope of this thesis, are:

- *Charge Conservation*: $\mathbf{E} = -\nabla \cdot V$, $\nabla \cdot (\varepsilon_0 \varepsilon_{\mathrm{r}} \mathbf{E}) = \rho_{\mathrm{F}}$ and $\mathbf{D} = \varepsilon_0 \varepsilon_{\mathrm{r}} \mathbf{E}$.
- *Zero Charge*: $\mathbf{n} \cdot \mathbf{D} = 0 \ \forall \ \mathbf{x} \in \partial\Omega$, where $\partial\Omega$ is the boundary of the selected domain Ω.
- *Initial Values*: $V(\mathbf{x}) = 0 \ \forall \ \mathbf{x} \in \Omega$, where Ω is the volume of the selected domain.
- *Electric Potential*: $V(\mathbf{x}) = V_0 \ \forall \ \mathbf{x} \in S$, where S is the selected surface.
- *Floating Potential*: $\int_{\partial\Omega} \mathbf{D} \cdot \mathbf{n} \mathrm{d}S = Q_0$, where $\partial\Omega$ is selected surface, $\mathbf{n}$ is the unit vector perpendicular to the infinitesimal surface area $\mathrm{d}S$ in $\partial\Omega$ and Q_0 is the total charge of the surface.

When the *Electrostatics* interface is added, the default nodes *Charge Conservation*, *Zero Charge* (default boundary conditions) and *Initial Values* are also added to the Model Builder.

The *Initial Values* node adds an initial value of the electric potential $V(\mathbf{x})$, which is by default 0 V, for each point in the selected volume Ω. The first default boundary condition *Charge Conservation* considers Gauss's law for the electric displacement field $\nabla \cdot (\varepsilon_0 \varepsilon_{\mathrm{r}} \mathbf{E}) = \rho_{\mathrm{F}}$ and also provides an interface for defining the constitutive relation $\mathbf{D} = \varepsilon_0 \varepsilon_{\mathrm{r}} \mathbf{E}$ and its associated properties such as the relative permittivity ε_{r}. As already shown in subsection 2.2.1, the scalar permittivity requires an isotropic material, which is generally not true for solid crystals. In *Charge Conservation*, it can be selected whether the relative permittivity of the material ε_r is taken from the material and isotropy is assumed or ε_r is user-defined. In this case, the components of the tensor ε_r can be individually inserted. This feature has not been used within the frame of this diploma thesis.

The *Zero Charge* node adds the condition that there is zero charge on the boundary of the selected domain.

A surface S, which is held at a constant electric potential $V = V_0 \neq 0$, can be realized with the *Electric Potential* node by selecting this boundary in the geometry and assigning a certain value for the electric potential V_0 to it. This overrides the zero charge boundary condition for the respective surface.

The *Floating Potential* node provides that the potential of the surface is only defined by the environment and the surrounding field and not by, for example, removing current in the case of grounded electrodes.

Other Features

Additionally, the following features of the *Electrostatics* interface have also been used:

- *Force Calculation*: $\mathbf{F} = \int_{\partial\Omega} \mathbf{n} T \mathrm{d}S$, where $\mathbf{n}$ is the unit vector perpendicular to an infinitesimal area $\mathrm{d}S$ of the surface $\partial\Omega$ and where T is the Maxwell stress tensor.

- *Space Charge Density*: $\nabla \cdot \mathbf{D} = \rho_\mathrm{F} \ \forall \ \mathbf{x} \in \Omega$, where ρ_F is the free space charge density and Ω is the selected volume.

- *Surface Charge Density*: $\mathbf{n} \cdot (\mathbf{D}_1 - \mathbf{D}_2) = \sigma_\mathrm{F} \ \forall \ \mathbf{x} \in S$, where σ_F is the free surface charge density and S is the selected surface.

The *Force Calculation* node allows to calculate the electrostatic force acting on a domain Ω in an external electric field. The Maxwell stress tensor for the force calculation generally represents the interaction between electromagnetic forces and mechanical momentum [36]. If the field is only electric, the Maxwell stress tensor becomes $T = \sigma_{ij} = \varepsilon \cdot (E_i E_j - \frac{1}{2} E_i E_i)$.

2.2.3 Basics of Electric Currents

An electric current is a net flow of charge due to the motion of charged particles and, hence, belongs to the field of electrodynamics [37]. The current in a thin conducting wire is a simple example. The electric current I is defined as the charge per unit time going through the cross-section of the wire A:

$$I = \frac{\mathrm{d}Q}{\mathrm{d}t}, \tag{2.33}$$

where $\mathrm{d}Q$ denotes the net charge going through the area A during the infinitesimal time interval $\mathrm{d}t$. If the charges q with a charge density n_L (= number of charges per unit length) moving with mean velocity v generate the current in the wire, the current becomes

$$I = qn_{\mathrm{L}}v. \tag{2.34}$$

Current Density and Continuity Equation

In order to describe the current at a point in the material, the volume current density $\mathbf{J}(\mathbf{x})$ is introduced. The definition of $\mathbf{J}(\mathbf{x})$ is that if $\mathrm{d}\mathbf{A}$ is an infinitesimal area at $\mathbf{x}$ in the volume, then $\mathbf{J}(\mathbf{x}) \cdot \mathrm{d}\mathbf{A}$ is the net charge $\mathrm{d}I$ per unit time passing through $\mathrm{d}\mathbf{A}$. If charges q with a charge density n_{V} (= number of charger per unit volume) move with mean velocity v, the volume current density is

$$\mathbf{J} = qn_{\mathrm{V}}\mathbf{v}. \tag{2.35}$$

If charges go out of the volume V through the closed surface ∂V, the overall charge enclosed by the volume V decreases according to the following equation

$$I = \int_{\partial V} \mathbf{J}\mathrm{d}\mathbf{A} = -\frac{\partial}{\partial t}\int_V \rho \mathrm{d}V. \tag{2.36}$$

The following equation of continuity can be derived by using Gauss's law [33]:

$$\nabla \cdot \mathbf{J}(\mathbf{x}, t) = -\frac{\partial}{\partial t}\rho_{\mathrm{el}}(\mathbf{x}, t), \tag{2.37}$$

which states that charge is not only conserved overall in a system, it is also conserved for every point in the system.

Ohm's law

If two terminal points of a conductor are held at a constant potential difference U, a steady current flows through the conductor. Within the time τ between successive collisions, one particle with mass m and charge q takes up an additional velocity $\mathbf{v} = \frac{q\tau\mathbf{E}}{m}$ in response to the electric field which is generated by the potential difference U. The relationship between the volume current density to the external electric field, which is also called the local form of Ohm's law, is given by

$$\mathbf{J} = n_{\mathrm{V}}q\mathbf{v} = \frac{n_{\mathrm{V}}q^2\tau}{m}\mathbf{E} = \sigma_{\mathrm{el}}\mathbf{E}, \tag{2.38}$$

where $\sigma_{\mathrm{el}} = \frac{n_{\mathrm{V}}q^2\tau}{m}$ is the electric conductivity of the material. It is inversely proportional to the resistivity $\rho_{\mathrm{el}} = \frac{1}{\sigma_{\mathrm{el}}}$ of the material. $\mathbf{J} = \sigma_{\mathrm{el}}\mathbf{E}$ is one of the so-called constitutive relations which describe the macroscopic properties of the medium.
In order to get the global form of Ohm's law, a conductor with volume V_0, a constant cross-section A, length L and an applied voltage U is considered: With $\int_{V_0} \mathbf{J}\cdot\mathrm{d}\mathbf{A}\cdot\mathrm{d}L = IL$ and $\int_{V_0} \mathbf{J} \cdot \mathrm{d}\mathbf{A} \cdot \mathrm{d}L = \int_{V_0} \sigma_{\mathrm{el}}\mathbf{E}\mathrm{d}V = \sigma_{\mathrm{el}}E \int_A \mathrm{d}A \int_L \mathrm{d}L = \sigma_{\mathrm{el}}ALE = \sigma_{\mathrm{el}}AU$, one gets

$$IL = \sigma_{\mathrm{el}} AU \Leftrightarrow U = \frac{IL}{\sigma_{\mathrm{el}} A} = RI, \tag{2.39}$$

where $R = \frac{L}{\sigma_{\mathrm{el}} A} = \frac{\rho_{\mathrm{el}} L}{A}$ is the resistance of this box-shaped conductor.

2.2.4 Electric Currents Interface in COMSOL

The *Electric Currents* interface models electric currents in conductive media and solves for the electric potential which is, hence, the dependent variable of this physics type [38].

Equations to be solved

The equations, which are solved in the *Electric Currents* interface, are

$$\nabla \cdot \mathbf{J} = Q_{\mathrm{J}}, \tag{2.40}$$

$$\text{and } \mathbf{J} = \sigma_{\mathrm{el}} \mathbf{E} + \mathbf{J}_{\mathrm{e}}, \tag{2.41}$$

$$\text{and } \mathbf{E} = -\nabla V, \tag{2.42}$$

where $\mathbf{J}_{\mathrm{e}}$ is the externally generated volume current density and Q_{J} is the change of the overall charge in the selected domain due to the electric current density. Eq. (2.40) represents the continuity equation, Eq. (2.41) the generalized Ohm's law and Eq. (2.42) is the relationship between the electric field and electric potential which is also used in the *Electrostatics* interface. As a result of Eq. (2.41), the electrical conducticity of the material needs to be known, in addition to the relative permittivity.

Boundary Conditions and Additional Features

The main condition at interfaces between different media and interior boundaries is continuity of the volume current density:

$$\mathbf{n}_2 \cdot (\mathbf{J}_1 - \mathbf{J}_2) = \mathbf{0} \; \forall \; \mathbf{x} \in S, \tag{2.43}$$

where $\mathbf{J}_1$ and $\mathbf{J}_2$ are the current densities in the volumes Ω_1 and Ω_2, which are separated by the interface S, and $\mathbf{n}_2$ is the unit vector perpendicular to S.

Further applied boundary conditions are:

- *Current Conservation*: $\nabla \cdot \mathbf{J} = Q_{\mathrm{J}}$, $\mathbf{J} = \sigma_{\mathrm{el}} \mathbf{E} + \mathbf{J}_{\mathrm{e}}$ and $\mathbf{E} = -\nabla \cdot V$.
- *Electric Insulation*: $\mathbf{n} \cdot \mathbf{J} = 0 \; \forall \; \mathbf{x} \in S$, where S is the selected boundary.
- *Initial Values*: $V(\mathbf{x}) = 0 \; \forall \; \mathbf{x} \in \Omega$, where Ω is the selected volume.

- *Electric Potential*: $V(\mathbf{x}) = V_0 \; \forall \; \mathbf{x} \in S$, where S is the selected boundary.

The *Current Conservation* node adds the continuity equation for the electric potential and provides an interface for defining the constitutive relations $\mathbf{J} = \sigma_{\mathrm{el}}\mathbf{E}$ and $\mathbf{D} = \varepsilon_0\varepsilon_{\mathrm{r}}\mathbf{E}$ and its associated properties such as the electrical conductivity σ_{el} and the relative permittivity ε_{r}. Assuming isotropy of the material, these values are scalar, but in the case of anisotropic materials the individual components of the tensors ε_{r} and σ_{el} can also be defined by the user.

Electric Insulation provides that no electric current flows into the selected boundary S. The *Initial Values* and *Electric Potential* nodes of the *Electric Currents* interface provide the same features as the ones of the *Electrostatics* interface, which are explained in subsection 2.2.2.

Other applied features of *Electric Currents* are *Force Calculation* and *Terminal. Force Calculation* is already explained in subsection 2.2.2, while *Terminal* is used to specify a constant current in a selected boundary. For a disconnected electrode in an external electric field, like a non-grounded conducting sphere in an external electric field, zero current needs to be specified. Therefore, the *Electric Currents* feature *Terminal* is similar to *Floating Potential* of *Electrostatics.*

2.2.5 Electric Currents, Shell Interface in COMSOL

The *Electric Currents, Shell* interface models steady electric currents in thin current-conducting shells and solves for the electric potential [39]. In order to simulate the MEMS transducer of the electric field microsensor, structures with thicknesses in the micrometer to submicrometer range are of interest. While meshing of domains with thicknesses down to 45 μm is not problematic, meshing down to 100 nm is very challenging, either impossible or extremely time-consuming. In this interface, a thin conducting structure is realized by a boundary with a shell of a thickness representing the thickness of the structure. In general, this physics type is similar to the 2D *Electric Currents* interface, solving for the electric potential on 2D surfaces in a 3D geometry, with the difference that the shell does not have to be flat but can have a certain shell thickness.

Equations to be solved

The equations, which are solved in the *Electric Currents, Shell* interface, are

$$\nabla_{\mathrm{T}} \cdot (d_{\mathrm{S}}\mathbf{J}) = d_{\mathrm{S}}Q_{\mathrm{J}}, \tag{2.44}$$

$$\text{and} \;\; \mathbf{J} = \sigma_{\mathrm{el}}\mathbf{E} + \mathbf{J}_{\mathrm{e}}, \tag{2.45}$$

$$\text{and} \;\; \mathbf{E} = -\nabla_{\mathrm{T}}V, \tag{2.46}$$

where ∇_{T} is the tangential derivative along the shell, d_{S} is the shell thickness and Q_{J} is an external current source. For the solution of these equations, the relative permittivity and the electrical conductivity of the material need to be known.

Boundary Conditions and Other Features

The required boundary conditions are:

- *Current Conservation*
- *Electric Insulation*
- *Initial Values*
- *Electric Potential*

As *Electric Currents, Shell* is similar to the 2D *Electric Currents* interface, these features are similar to the features of *Electric Currents* which are explained in subsection 2.2.4.

2.3 Example: Conducting Spheres in a Constant Electric Field

In this example, a grounded conducting sphere of radius a is centered at the origin, in an externally applied electric field $E_0^i(x^m) = E_0 \cdot e_{\mathrm{z}}^i$, where e_{z}^i is the unit vector in the z-direction.

The presence of the sphere changes the field. By solving this problem analytically, the potential $V(x^m)$, the electric field $E^i(x^m)$, the charge density of the sphere's surface $\sigma(x^m)$ and the force on the hemispheres can be determined. This analytical solution is used to examine the precision of COMSOL simulations of this problem.

2.3.1 Analytical Solution of One Conducting Sphere in a Constant Electric Field

In subsection 2.2.1, the electric potential in the presence of a conducting sphere of radius a and charge Q_0 has already been determined by solving Laplace's equation in spherical coordinates. The general solution of the second-order differential equation of this problem for $r \in [a, \infty)$ is $V(r) = \frac{A}{r} + B$.

The influence of the external electric field on the general solution of the electric potential can be calculated by integrating E_0^i since $E^i = -\partial_i V$. As E_0^i only depends on z, this part of the electric potential reduces to $V_0 = -E_0 z = -E_0 r \cos\theta$ so that the general solution of the electric potential for this problem is now: $V(r) = \frac{A}{r} + B + Cr\cos\theta$.

Furthermore, the free electrons of the conductor move in response to the electric force $F^i = -eE^i$ until a new equilibrium is reached, which happens when $E^i = 0^i$ inside the conductor. This induces an electric dipole in the sphere that is formed by two equal but opposite charges $q_1 = q$ and $q_2 = -q$ with distance d [32]. In the limit $d \to 0$ and by taking the origin to be the position of the dipole, all multipole moments except for the dipole moment $p^i = qde^i_{\mathrm{z}}$ are zero. The potential of a point-like dipole is generally given by $V(x^m) = \frac{p^i x^i}{4\pi\varepsilon_0 r^3} = \frac{1}{4\pi\varepsilon_0}\frac{p_{\mathrm{z}} z}{r^3} = \frac{1}{4\pi\varepsilon_0}\frac{p_{\mathrm{z}}\cos\theta}{r^2}$. Considering this contribution to the electric potential, the general solution of the electric potential for this problem finally becomes

$$V(x^m) = A + \frac{B}{r} + Cr\cos\theta + \frac{D}{r^2}\cos\theta. \tag{2.47}$$

The arbitrary constant A can be set equal to 0. Furthermore, for any positive charge residing on the sphere above the $z = 0$ plane, an equal amount of negative charge will appear below it. This makes the total surface charge zero so that $B = 0$. The boundary conditions for determining the constants C and D are

$$\lim_{r\to\infty} V(x^m) = V_0(r) = -E_0 r\cos\theta, \tag{2.48}$$

$$\text{and} \;\; V(x^m) = 0 \;\forall\; x^m \text{ with } r = a. \tag{2.49}$$

Eq. (2.48) leads to $C = -E_0$ and Eq. (2.49) to $D = E_0 a^3$ so that the final solution of the electric potential becomes

$$V(r,\theta) = -E_0 r\cos\theta + \frac{E_0 a^3\cos\theta}{r^2}. \tag{2.50}$$

The electric field can be calculated by $E^i = -\partial_i V$, but as $V(r,\theta)$ is given in spherical coordinates the gradient needs to be transformed into this coordinate system. In subsection 2.2.1, the Laplacian operator has already been transformed into the spherical coordinate system by inserting the scale factors $h_{\mathrm{r}} = 1$, $h_\theta = r$ and $h_\phi = r\sin\theta$ into the relevant equation for the Laplacian operator in a curvilinear coordinate system. The equation for the gradient in an arbitrary curvilinear coordinate system with the scale factor h_i and $i = 1,2,3$ is

$$e^i_\alpha \partial_i f = \frac{1}{h_{\underline{\alpha}}}\partial_{\underline{\alpha}} f, \tag{2.51}$$

where e^i_α for $i = 1,2,3$ are the unit vectors in the directions of independent positive displacements of the coordinates. $\underline{\alpha}$ indicates that the Einstein summation convention is not applied for this index although it is repeated. By inserting the relevant scale factors h_{r}, h_θ and h_ϕ, the gradient in the spherical coordinate system becomes

$$\partial_i f = \partial_{\mathrm{r}} f \cdot e^i_{\mathrm{r}} + \frac{1}{r}\partial_\theta f \cdot e^i_\theta + \frac{1}{r\sin\theta}\partial_\phi f \cdot e^i_\phi. \tag{2.52}$$

So, the electric field can be calculated by $E^i = -\partial_i V$ with the electric potential V from Eq. (2.50) and with the gradient in spherical coordinates from Eq. (2.52):

$$E^i(x^m) = \left(\frac{2E_0 a^3 \cos\theta}{r^3} + E_0 \cos\theta\right) \cdot e^i_{\mathrm{r}} + \left(\frac{E_0 a^3 \sin\theta}{r^3} - E_0 \sin\theta\right) \cdot e^i_{\theta}. \tag{2.53}$$

The surface charge density of the conducting sphere can be calculated via the boundary condition of the electric field in electrostatics, given in Eq. (2.12):

$$E^1_{\perp} - E^2_{\perp} = \frac{\sigma(x^m)}{\varepsilon_0} \; \forall \, x^m \in S, \tag{2.54}$$

where $E^1_{\perp}$ and $E^2_{\perp}$ are the electric field components (in the volumes V_1 and V_2), which are perpendicular to the surface S that separates V_1 and V_2. With the assumption that E^2 is the electric field inside the conductor and, hence, zero, the surface charge density is given by

$$\sigma(x^m) = \varepsilon_0 E^i(x^m)|_{r=a} \cdot n^i = 3\varepsilon_0 E_0 \cos\theta e^i_{\mathrm{r}} e^i_{\mathrm{r}} = 3\varepsilon_0 E_0 \cos\theta, \tag{2.55}$$

where n^i is the unit vector perpendicular to the surface of the sphere which points in radial direction. Therefore, only the part of the electric field pointing in radial directon e^i_{r} contributes to the surface charge density. The total surface charge, which is given by $Q_{\mathrm{tot}} = \int_0^{\pi} \sigma(\theta) 2\pi a^2 \sin\theta \mathrm{d}\theta$, is 0 which was originally surmised. The result $Q_{\mathrm{tot}} = 0$ leads to the fact that no charge is transferred between the sphere and ground. Therefore, the grounded sphere can be replaced by an uncharged isolated sphere in the original statement of the problem and the same results (2.50), (2.53) and (2.55) still hold.

If an electric field is applied to a conductor, the forces acting on the conductor are only exerted on its surface because the charges are accumulated there in the electrostatic equilibrium. The force $\mathrm{d}F^i$ on a surface area $\mathrm{d}A$ of the conductor, which has already been introduced in subsection 2.2.1, is

$$\mathrm{d}F^i = \frac{\sigma(x^m)^2}{2\varepsilon_0} \mathrm{d}A \cdot n^i, \tag{2.56}$$

where n^i is the unit vector perpendicular to $\mathrm{d}A$. Due to the symmetry of the problem, there is only a net force in z-direction on the upper and on the lower hemisphere, respectively. The net force on the upper hemisphere, which is located in $z \geq 0$, is

$$\begin{aligned} F_z(\text{upper}) = \int \mathrm{d}F \cos\theta \mathrm{d}V &= \int_0^{2\pi} \mathrm{d}\phi \int_0^{\frac{\pi}{2}} a^2 \sin\theta \mathrm{d}\theta \cdot \frac{9{\varepsilon_0}^2 {E_0}^2 \cos^3\theta}{2\varepsilon_0} \\ &= 9\pi\varepsilon_0 {E_0}^2 a^2 \int_0^{\frac{\pi}{2}} \sin\theta \cos^3\theta \mathrm{d}\theta = \frac{9\pi\varepsilon_0 {E_0}^2 a^2}{4}. \end{aligned} \tag{2.57}$$

The net force on the lower sphere, which is located in $z \leq 0$, is

$$F_z(\text{lower}) = \frac{9\pi\varepsilon_0 {E_0}^2 a^2}{4}. \tag{2.58}$$

2.3.2 COMSOL Simulation of One Conducting Sphere in a Constant Electric Field

In order to simulate a conducting sphere of radius a, centered at origin, in an externally applied constant electric field, the following parameters are set in COMSOL Multiphysics:

Parent node	**Subnode**	**Feature**	**Important feature settings**
Global Definitions	Parameters	Parameter initialization	$a = 0.0003$[m] (radius of sphere), $length = 0.006$[m], $width = 0.003$[m], $height = 0.003$[m], $E_0 = 100$[V/m], $U = 0.5 \cdot E_0 \cdot length[V]$, $mesh\_param = 30$
Component	Geometry	Sphere 1	Type = solid, radius = a, position = (0,0,0), axis type = z-axis
Component	Geometry	Block 1	Type = solid, size = ($width$,$length$,$height$), center = (0,0,0)
Component	Geometry	Block 2	Type = solid, size = ($width$,$length$,$height$), center = (0,$length$/2,0)
Component	Geometry	Intersection	Input objects = (Sphere 1, Block 2)
Component	Geometry	Mirror 1	Input object = Intersection, keep input objects, point on plane of reflection = (0,0,0), normal vector to plane of reflection = (0,1,0)
Component	Materials	Air	Relative permittivity = 1, domain selection = all domains but sphere (overridden by material copper)
Component	Materials	Copper	Relative permittivity = 1, domain selection = Sphere 1
Component	Electrostatics (es)	Charge Conservation	Domain selection = all domains
Component	Electrostatics (es)	Zero Charge	Boundary selection = all boundaries
Component	Electrostatics (es)	Initial Values	Initial Value = 0 V, Domain Selection = All domains
Component	Electrostatics (es)	Electric Potential 1	$V_0 = U$, Boundary selection = first end face of rectangular Block 1 at $y = -length/2$
Component	Electrostatics (es)	Electric Potential 2	$V_0 = -U$, Boundary selection = second end face of rectangular Block 1 at $y = length/2$

Component	Electrostatics (es)	Floating Potential	Boundary selection = boundaries of the sphere
Component	Electrostatics (es)	Force Calculation 1	Domain selection = first hemisphere in $y > 0$, force name = Fesuppersphere
Component	Electrostatics (es)	Force Calculation 2	Domain selection = second hemisphere in $y < 0$, force name = Feslowersphere
Component	Mesh	Free Triangular	Boundary selection = boundaries of Sphere 1, element size = extremely fine, maximum element size = $a/mesh\_param$
Component	Mesh	Free Tetrahedral	Domain selection = remaining, element size = normal
Results	Derived Values	Global Evaluation	Label = "Force on upper hemisphere", evaluate y-component of calculated force "Fesuppersphere"
Results	Derived Values	Global Evaluation	Label = "Force on lower sphere", evaluate y-component of calculated force "Feslowersphere"
Results	Derived Values	Global Evaluation	Label = "Analytical solution for force on hemisphere", evaluate expression $\frac{9\varepsilon_0 {E_0}^2 a^2 \pi}{4}$
Results	Tables	Overview Forces	The derived values "Force on upper hemisphere", "Force on lower hemisphere" and "Analytical solution for force on hemisphere" are evaluated in this table
Results	Electric Potential (es)	Multislice	Number of x-/y-/z-planes = (1,1,1)

In order to calculate the electric force on one hemisphere, the sphere in the middle of *Block 1* needs to be cut into two separate domains. This is done by building a second block *Block 2* in such a way that the intersection of the domains *Sphere 1* and *Block 2* is a hemisphere. This hemisphere is then mirrored, while the input object is kept, in order to build up a complete sphere.

The relative permittivities of the materials *Copper* which is assigned to the conducting sphere and *Air* which is assigned to the remaining geometry are set to 1.

The electric potential U and $-U$ of the *Block 1* end faces are set in such a way that the constant external electric field acting on the sphere is 100 V/m.

For the user-controlled mesh, it is generally important that the smallest objects in the geometry with the finest mesh elements are meshed previous to larger objects. In this case, the surface of *Sphere 1* is meshed extremely fine with a customized maximum mesh element size of $a/mesh\_param$. Then the mesh elements of the remaining geometry are generated with respect to the smallest mesh elements.

The *Results* node offers many opportunities for plotting the electric potential and the multislice plot is shown in Fig. 2.3 as an example.

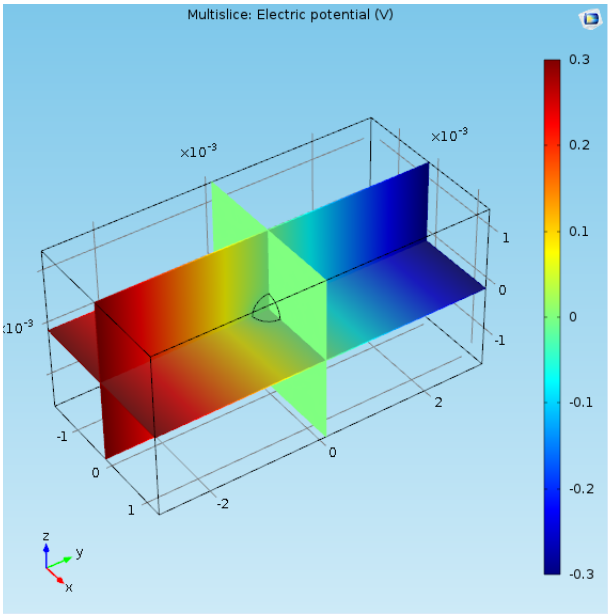

Figure 2.3: Multislice plot of the calculated electric potential in V for the conducting sphere in a constant outer electric field.

Figure 2.3 reveals that due to the approximately constant electric field throughout the geometry the electric potential exhibits a linear decrease in the positive y-direction. This can also be derived from $\mathbf{E} = -\nabla V$. A closer look on the sphere's proximity is illustrated in Fig. 2.4 and reveals that the electric field is not constant. The electric field distortions have several reasons, which have already been introduced in subsection 2.2.1. On the one hand, the electric field inside the conductor is zero and, hence, the electric potential is constant. On the other hand, the electric field needs to be perpendicular to the conductor's surface. In Fig. 2.4, the radius of the sphere has been varied from 0.3 mm to 1 mm to illustrate that larger conducting bodies lead to more severe distortions of the electric field. This shows one motivation for the novel electric field sensing principle, where the conductive materials are limited to the micro-electro-mechanical transducer. Due to the small dimensions of the E-field sensing element, there are only minor distortions confined to the vicinity of the transducer and long-ranging E-fields are scarcely affected. However, one also has to consider that the forces on the MEMS elements decrease significantly according to $F \propto a^2$, where a is the radius of the element. For example, decreasing the radius by a factor of 10 leads to a decrease of the electric force by a factor of 100. Therefore, the design of such a MEMS transducer must be optimized to maintain a reasonable sensitivity.

The global evaluations for the analytical and simulated forces with the mesh settings described above are summarized in Table 2.2. There are only small deviations

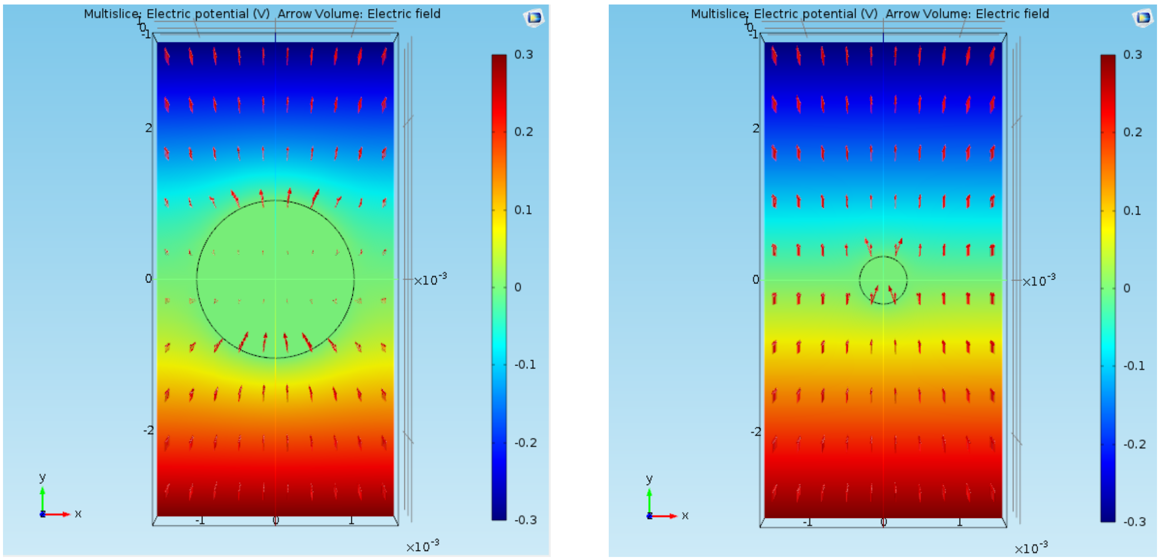

(a) (b)

Figure 2.4: Electric potential and electric field vectors in the x-y-plane for a sphere with radius (a) $a = 1$ mm and (b) $a = 0.3$ mm.

Table 2.2: Comparison of analytically calculated and simulated forces in fN. The radius of the sphere is 0.3 mm.

Analytical solution for force on upper hemisphere in fN	Simulated force on upper hemisphere in fN (relative difference to analytical value)	Simulated force on lower hemisphere in fN (relative difference to analytical value)
56.328	56.022(−0.54%)	−56.022(−0.54%)

from the analytical solutions because of the highly symmetric problem and the predefined *extremely fine* meshing of the sphere. The maximum mesh element size is set to *radius/mesh* while the other element size parameters are automatically generated by the predefined extremely fine meshing. Furthermore, the simulated forces on the two hemispheres are equal, which is also in accordance with the theory.

To investigate the influence of the meshing quality on the simulation accuracy, a sweep for the meshing parameter *mesh_param* in the range of 5 to 30 with steps of 5 has been carried out and the results of this study is summarized in Table 2.3. The mesh parameter defines the maximum mesh element size of the *Free Triangular* mesh of the sphere's surface by *radius/mesh_param*. It can be seen that the finer the mesh, the more accurate the simulation. However, finer meshing can significantly increase the computation time. For this highly symmetric problem, however, this effect is only minimal.

Table 2.3: Comparison of analytically calculated and simulated forces fN for different meshing qualities. The parameter *mesh_param* defines the maximum mesh element size of the *Free Triangular* mesh of the sphere's surface by $(radius)/mesh\_param$. The radius of the sphere is 0.3 mm.

mesh_param	Simulated force on upper hemisphere in fN (relative difference to analytical value)	Simulated force on lower hemisphere in fN (relative difference to analytical value)
5	$55.377(-1.69\%)$	$-55.365(-1.71\%)$
10	$55.847(-0.85\%)$	$-55.8505(-0.85\%)$
15	$55.959(-0.66\%)$	$-55.958(-0.66\%)$
20	$55.994(-0.59\%)$	$-55.993(-0.59\%)$
25	$56.015(-0.56\%)$	$-56.013(-0.56\%)$
30	$56.022(-0.54\%)$	$-56.022(-0.54\%)$

2.3.3 COMSOL Simulation of Two Conducting Spheres in a Constant Electric Field

In general, the electro-mechanical transduction principle of the electric field microsensor is based on the interaction between two conductors in an externally applied constant electric field. To get a feeling for these interactions, the simple problem of two conducting spheres in an outer electric field is investigated. Additionally to the settings of the COMSOL simulation for one conducting sphere, which are described in subsection 2.3.2, the features listed in Table 2.4 have been added or changed. It is assumed for this step that the two conductive bodies are insulated.

A sweep of the parameter *rel_dist*, which defines the distance between the centers of the spheres relative to the radius a, has been carried out with steps of 0.25 in the range of 0.25 to 12. The net forces acting on the two spheres for different distances are summarized in Fig. 2.5a: Two electrically insulated spheres are subject to attractive net forces, if the distance between them is small. For larger distances, the forces decrease according to $1/d^2$. For example, at $rel\_dist = 4$ the attractive forces are already almost zero.

Two electrically connected spheres can be simulated by putting the boundaries of the two spheres on one *Floating Potential*. The net forces acting on the two connected spheres for different distances are summarized in Fig 2.5b and show that there is always a repulsive force which increases linearly with increasing distance.

As two electrically connected conductors generally become oppositely charged in an external electric field, the field is neutralized beween the conductors. This is illustrated in Fig. 2.6.

The force $\mathrm{d}F^i$ on a surface area $\mathrm{d}A$ of a conductor is given in Eq. (2.56) and, amongst others, depends on the surface charge density. The surface charge density is determined by Eq. (2.54) and depends on the electric field components inside and outside the conductor in the proximity of the respective surface area $\mathrm{d}A$. For the surfaces adjacent to the field-free region, all these components are zero so that not only the surface charge

Table 2.4: Additional features to the settings in subsection 2.3.2 for the COMSOL simulation of two insulated conducting spheres.

Parent node	**Subnode**	**Feature**	**Important feature settings**
Global Definitions	Parameters	Parameter initialization	$a = 300[\mu m]$ (radius of the spheres), $rel\_dist = 1$ (distance between the spheres relative to the radius), $d = a \cdot (rel\_dist + 2)$ (distance between the centers of the two spheres)
Component	Geometry	Sphere 1	Type = solid, radius = a, position = (0,0,0), axis type = z-axis
Component	Geometry	Move 1	Input object = 2 hemispheres, displacement = (0,$d/2$,0)
Component	Geometry	Mirror 2	Input object = 2 hemispheres after Move 1, keep input objects, point on plane reflection = (0,0,0), normal vector to plane of reflection = (0,1,0)
Component	Electrostatics (es)	Floating Potential 1	Boundary selection = boundaries of Sphere 1 at $y = -d/2$
Component	Electrostatics (es)	Floating Potential 2	Boundary selection = boundaries of Sphere 2 at $y = d/2$
Component	Electrostatics (es)	Force Calculation 1	Domain selection = hemisphere of Sphere 1 in -y-direction, force name = Fes11
Component	Electrostatics (es)	Force Calculation 2	Domain selection = hemisphere of Sphere 1 in +y-direction, force name = Fes12
Component	Electrostatics (es)	Force Calculation 3	Domain selection = hemisphere of Sphere 2 in -y-direction, force name = Fes21
Component	Electrostatics (es)	Force Calculation 4	Domain selection = hemisphere of Sphere 2 in +y-direction, force name = Fes22
Component	Mesh	Free Triangular	Boundary selection = boundaries of Sphere 1 and Sphere 2, element size = extremely fine, maximum element size = $a/10$

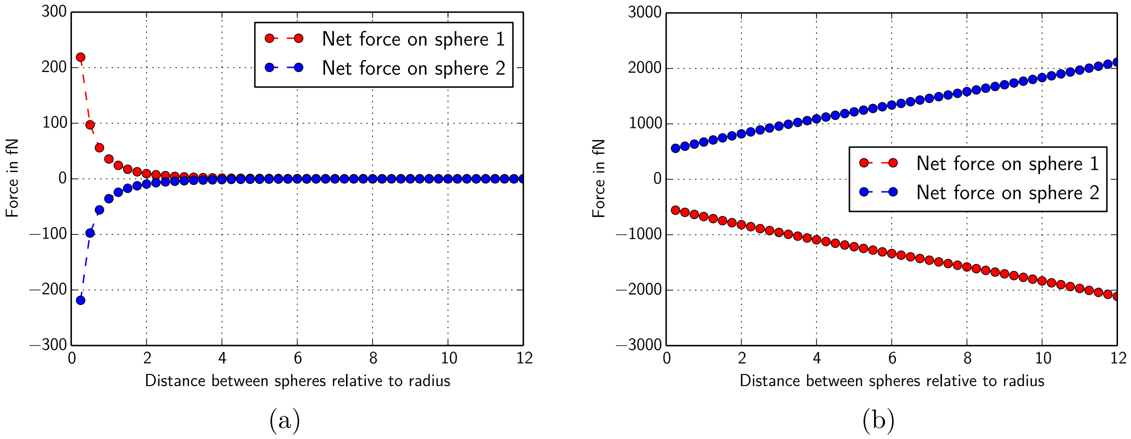

Figure 2.5: Net forces on two electrically (a) insulated and (b) connected spheres in an external constant E-field of 100 V/m.

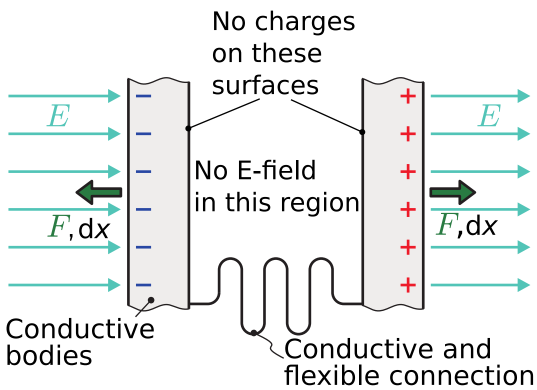

Figure 2.6: Two electrically connected conductive plates in an outer electric field E. The field-free region between the conductors due to charge separation leads to repulsive net forces F which try to further pull apart the plates.

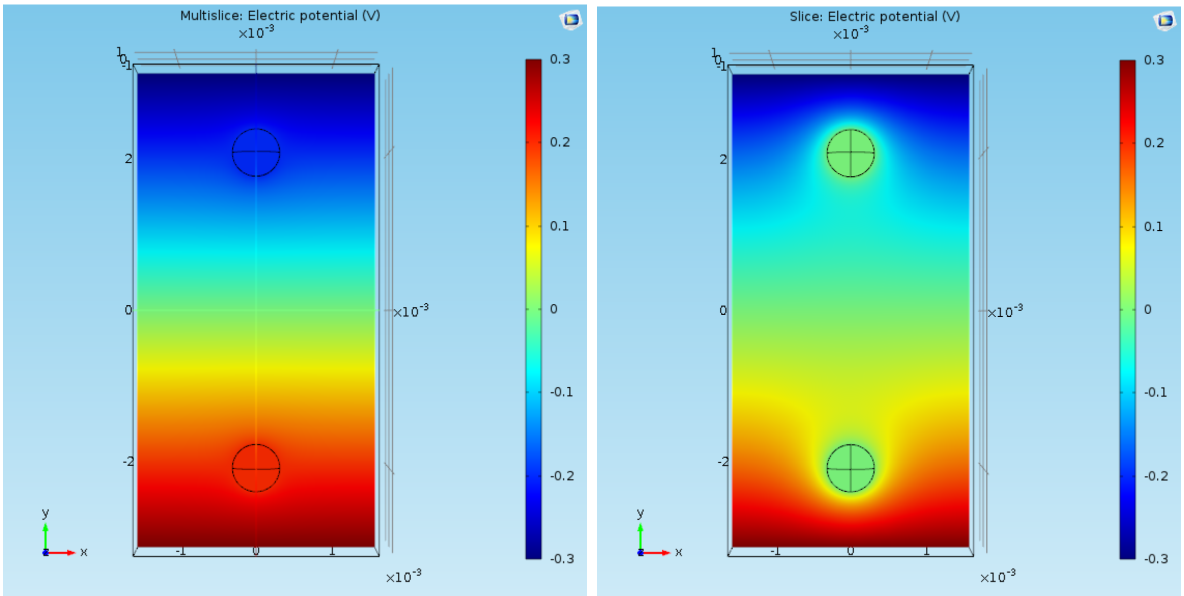

(a) (b)

Figure 2.7: Electric potentil in the x-y-plane for two electrically (a) insulated and (b) connected spheres in an external constant E-field of 100 V/m. The distance between the spheres relative to the radius is 10.

densities but also the forces on these surfaces are zero. Therefore, the repulsive forces, which are indicated in Fig. 2.6 by dark green arrows, remain.

Furthermore, electrical connection between two conductors leads to more severe electric field distortions which is illustrated in Fig. 2.7. In the case of electrical connection, the spheres are on one potential and as they are spatially separated in an outer constant electric field, they are located in regions where a large difference between the electric potential outside and inside the conductor is generated. Due to $\mathbf{E} = -\nabla V$, these large differences generate large E-fields in the respective regions and, hence, major field distortions. The effects of electrical connections on electric field distortions underline another important beneficial characteristic of the novel electric field sensing priniple: The MEMS transducer does not need any conductive connections to external bodies and, by using the optical readout with glass fibers, it is galvanically separated from the optoelectronic components.

2.4 Is Physics Type Electric Currents necessary for Simulations of Electric Field Sensors?

COMSOL Multiphysics offers physics interfaces for modeling static electric fields and currents. In order to determine the required physics interface for modeling, a basic understanding of the charge dynamics in conductors is required [40]. In general, if it is

Table 2.5: Suitable physics interfaces and study types for different time-scale regimes.

Case (Example)	**Physics interface**	**Study type**
$t \ll \tau$ (Insulator)	*Electrostatics*	Stationary
$t \gg \tau$ (Conductor)	*Electric Currents*	Stationary

not clear whether to use the *Electric Currents* (*ec*) or the *Electrostatics* (*es*) interface which both solve for the electric potential, the charge relaxation theory can be applied to understand the charge transport in conductors.

2.4.1 Charge Relaxation Theory

By combining Ohm's law $\mathbf{J} = \sigma_{\mathrm{el}}\mathbf{E}$, the equation of continuity $\nabla \cdot \mathbf{J} = -\partial\rho/\partial t$ and one of the Maxwell equations of electrostatics $\nabla \cdot \mathbf{D} = \nabla \cdot (\varepsilon\mathbf{E}) = \rho$ (see also subsection 2.2.1 and subsection 2.2.3), the following differential equation for the space charge density ρ in a homogenous medium is generated:

$$\frac{\partial\rho}{\partial t} + \frac{\sigma_{\mathrm{el}}}{\varepsilon}\rho = 0, \tag{2.59}$$

where σ_{el} is the electrical conductivity of the material and ε is the permittivity of the material. The solution of Eq. (2.59) is

$$\rho(t) = \rho_0 \cdot \exp(-t/\tau), \tag{2.60}$$

where

$$\tau = \frac{\varepsilon}{\sigma_{\mathrm{el}}} \tag{2.61}$$

is called the charge relaxation time. When modeling a real world device, there is not only the intrinsic time scale of charge relaxation time τ but also an external time scale t, at which the device is energized or observed. It is the relation between these two time scales that determines which physics interface and study type should be used. The suitable interfaces for different relationships between observation time t and charge relaxation time τ are summarized in Table 2.5.

If the observation time is much smaller than the charge relaxation time, the charges do not have enough time to redistribute to any significant degree. Thus, the charge distribution can be considered as the given model input and the *Electrostatics* interface is the best approach to solve for the electric potential. This is the case for insulators because their electrical conductivities are relatively small and their permittivities are relatively large, so that τ becomes large. For example, the charge relaxation time of a good insulator like silica glass is of the order of 10^3 s.

If the observation time is long compared to the charge relaxation time, a stationary solution of the equation of continuity $\nabla \cdot \mathbf{J} = -\partial\rho/\partial t$ has been reached, resulting in a

Table 2.6: Additional features to the settings in subsection 2.3.2 for the COMSOL simulation of one conducting sphere in a constant electric field. Considering the charge relaxation theory, *Electric Currents* is assigned to the sphere an *Electrostatics* is assigned to the surrounding medium.

Parent node	**Subnode**	**Feature**	**Important feature settings**
Component	Electrostatics (es)	Electric Potential 3	Boundary selection = all boundaries of Sphere 1, electric potential = dependent variable V of *Electric Currents*
Component	Electric Currents (ec)	Current Conservation	Domain selection = Sphere 1
Component	Electric Currents (ec)	Electric Insulation	Boundary selection = all boundaries of Sphere 1
Component	Electric Currents (ec)	Initial Values	Domain selection = Sphere 1, initial electric potential = 0 V
Component	Electric Currents (ec)	Electric Potential	Boundary selection = all boundaries of Sphere 1, electric potential = dependent variable $V2$ of *Electrostatics*

current. In a stationary coordinate system, Ohm's law states that $\mathbf{J} = \sigma_{\mathrm{el}}\mathbf{E} + \mathbf{J}_{\mathrm{e}}$. By combining these two equations, the static form of the equation of continuity becomes

$$\nabla \cdot \mathbf{J} = -\nabla \cdot (\sigma_{\mathrm{el}} \nabla V - \mathbf{J}_{\mathrm{e}}) = 0. \tag{2.62}$$

To handle current sources, the equation can be generalized to

$$-\nabla \cdot (\sigma_{\mathrm{el}} \nabla V - \mathbf{J}_{\mathrm{e}}) = Q_{\mathrm{J}}. \tag{2.63}$$

As this equation is used in the *Electric Currents* interface, this physics type is relevant for the situation, where $t \gg \tau$. For a good conductor like copper, τ is of the order of 10^{-19} s.

2.4.2 Spheres in a Constant Electric Field

As a result of the charge relaxation theory, this problem strictly needs *Electric Currents* for the conducting sphere and *Electrostatics* for the surrounding insulating air. For the simulation, additionally to the settings in subsection 2.3.2, the following most important features, which are summarized in Table 2.6, have been added or changed.

The two physics interfaces are coupled by setting the electric potential of *Electric Currents* V equal to the electric potential of *Electrostatics* $V2$ on the sphere's surface. While the relative permittivities of air and copper are 1, the electrical conductivity

Table 2.7: Forces on conducting hemispheres in a constant electric field generated by simulations using only *Electrostatics* (*es*) or combining *Electrostatics* with *Electric Currents* (*es+ec*). In the case of *es+ec*, the electric conductivity is varied in order to simulate conductors and semiconductors.

Physics (electric conductivity)	**Force on lower hemisphere in fN**	**Force on upper hemisphere in fN**
es (σ_{el} not necessary)	-56.020	56.019
es+ec ($\sigma_{\text{el}} = 5.998 \cdot 10^7$ S/m)	-56.021	56.019
es+ec ($\sigma_{el} = 0.01$ S/m)	-56.021	56.019
es+ec ($\sigma_{el} = 1.56 \cdot 10^{-3}$ S/m)	-56.019	56.018

additionally needs to be known for *Electric Currents* and is given by $5.9987 \cdot 10^7$ S/m for copper. The simulations of *es+ec* showed that the almost exact same force values as for *es* have been generated. Also, for materials which are not as conductive as silicon with $\sigma_{\text{el}} = 1.56 \cdot 10^3$ S/m, almost the same results were calculated. The force values for different physics combinations and electric conducitivities are listed in Table 2.7.

Within the scope of this diploma thesis, the results for the forces on the two hemispheres have also been compared. The results revealed only negligible differences. For the problem "conducting sphere in a constant electric field", there is obviously no difference between just applying *Electrostatics* (*es*) and combining *Electrostatics* with *Electric Current* (*es+ec*). Despite the same results, the computation of *es+ec* is much more time-consuming than just using *es*.

Furthermore, the simulation of two copper spheres in a constant electric field, which was already described in subsection 2.3.3, has also been carried out for the combination of *Electrostatics* and *Electric Currents*. In general, COMSOL compares the relative error to the relative tolerance for each iteration step during the computation and if the relative error is greater than the relative tolerance at any iteration step, the computation is stopped and the returned solution does not converge. It was shown that even for coarser meshing, like normal *Free Tetrahedral* mesh for all domains, an extremely large relative error of $2.1 \cdot 10^3$ was generated. The simulation with these settings failed to find a solution since the relative error was greater than the relative tolerance with the default value 0.001. Increasing the relative tolerance of the stationary solver to a value, which is greater than the relative error displayed in the error message, enabled the simulation to find a solution. In general, if the relative tolerance is not so tight, the returned solution diverges more from the actual solution due to the accumulation of the allowed relative errors at each iteration step.

However, increasing the relative tolerance is not the only possibility to address the problem: The simulations showed that the relatively large electrical conductivity of copper with $\sigma_{\text{el}} = 5.998 \cdot 10^7$ S/m caused this problem and that a decreasing σ_{el} lead

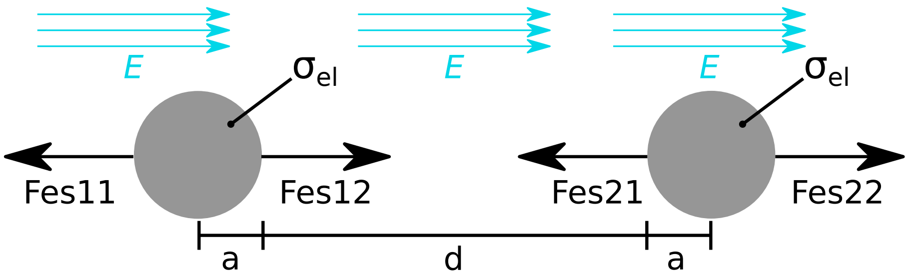

Figure 2.8: Illustration of two spheres with an electrical conductivity σ_{el} and radius a. The forces Fes11, Fes12, Fes21 and Fes22 are exerted on the 4 hemispheres, respectively, due to an external constant electric field E.

to a decreasing relative error which enabled the simulation to find a solution. For the default relative tolerance of 0.001, σ_{el} needs to be smaller than 0.01 S/m, while for a relative tolerance of 1 the electrical conductivity must be smaller than 10 S/m. For the electrical conductivity of copper $\sigma_{\mathrm{el}} = 5.998 \cdot 10^7$ S/m, the relative tolerance needs to be greater than 10^5. The basic setup of the simulation is illustrated in Fig. 2.8 and the resulting forces for these different settings are summarized in Table 2.8.

For the relatively small electric conductivities of semiconductors, the force values of *es+ec* are exactly the same as for *es* and due to the small relative tolerance of 0.001, the possibility of wrong results is minimal. Larger electrical conductivities need larger relative tolerances so that enables COMSOL can find a solution but wrong results are much more likely. Therefore, the force values of *es* in Table 2.8 can be assumed to be the right results.

2.4.3 U-Shapes in a Constant Electric Field

As a consequence of the last subsection, the physics interface *Electrostatics* properly simulates the highly symmetric problem of spheres in a constant electric field. An example for more complex geometries are two insulated u-shaped domains which are placed in a constant electric field.

The u-shaped geometry was imported from an external COMSOL Multiphysics file and transformed in such a way that the following geometry, illustrated in Fig. 2.9, was generated. The centroid of the two u-shapes is located in the center of a larger block.

Air is assigned to the block and *Silicon (single-crystal,isotropic)* is assigned to the u-shapes. The electric potential U and $-U$ of the block's end faces are set in such a way that the constant electric field inside the block becomes 100 V/m. In order to solve the problem only with *es*, the u-shapes are set on separate floating potentials. For *es+ec*, the two physics need to be coupled by setting the electric potential of *Electric Currents* V equal to the electric potential of *Electrostatics* $V2$ on the u-shapes' surfaces. For a parametric sweep, the following parameters are defined in *Global Definitions*:

- *x_displ* in m: Displacement of the u-shapes in x-direction,
- *scal*: Scaling of the u-shapes with a center of scaling at (0,0,0),

Table 2.8: Forces on the hemispheres of two spheres (with electric conductivities σ_{el}) in a constant electric field generated by simulations using only *Electrostatics* (es) or combining *Electrostatics* and *Electric Currents* (es+ec). In the case of *es+ec*, the electric conductivity is varied for simulations of conductors and semiconductors. The force values of *es* can be assumed to be the right results.

Physics (Settings)	**Fes11 in fN**	**Fes12 in fN**	**Fes21 in fN**	**Fes22 in fN**
es	−151.4	159.4	−156.0	150.0
es+ec ($\sigma_{\mathrm{el}} = 5.998 \cdot 10^7$ S/m, $T = 10^5$)	−590.8	29.2	−28.9	582.8
es+ec ($\sigma_{\mathrm{el}} = 100$ S/m, $T = 100$)	−178.9	119.6	−112.7	189.9
es+ec ($\sigma_{\mathrm{el}} = 1$ S/m, $T = 1$)	−151.4	159.3	−156.0	149.7
es+ec ($\sigma_{\mathrm{el}} = 0.01$ S/m, $T = 0.001$)	−151.4	159.4	−156.0	149.7

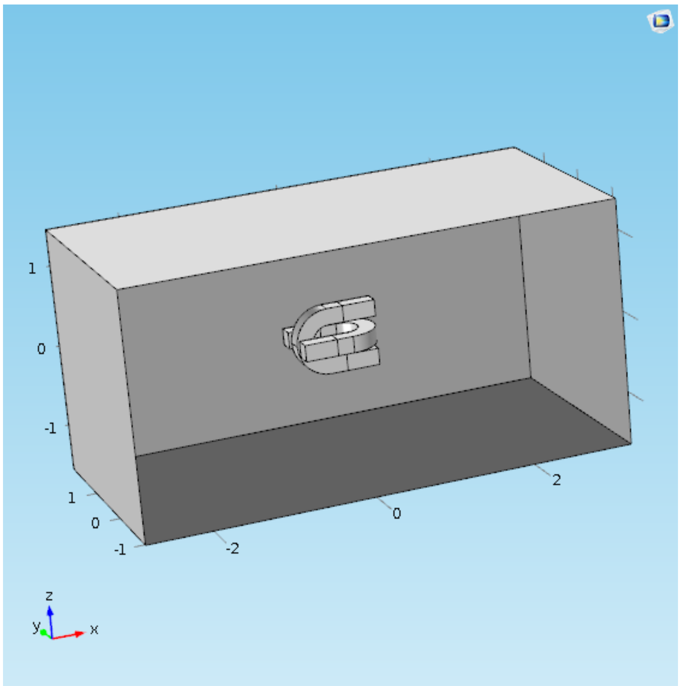

Figure 2.9: Illustration of the two u-shapes located in the center of a block.

- n: Switch between 0 (*es*) and 1 (*es*+*ec*).

The displacement and the scaling is done by inserting *x_displ* and *scal* in the *Geometry*'s features *Move* and *Scale*, respectively. For switching between *es* and *es*+*ec*, a box is created in *Definitions* in such a way that $n = 0$ makes the box disappear so that no domain is assigned to *ec*, while $n = 1$ creates a box that encloses the two u-shapes so that these entities inside the box are included in the selection and assigned to *ec*.

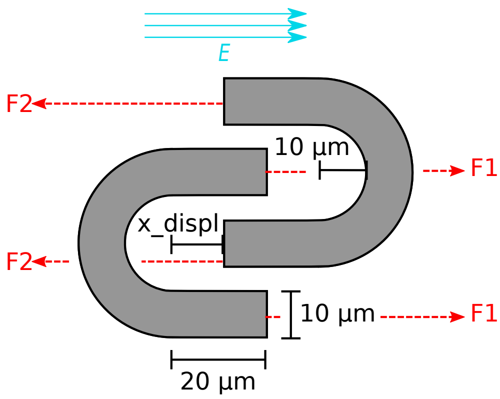

Figure 2.10: Illustration of two u-shapes in an external electric field E. The electromagnetic forces $F1$ and $F2$ act on the right and on the left u-shape, respectively.

A sweep for some combinations of different parameter values *x_displ*, *scal* and n showed that for each combination of *x_displ* and *scal* almost the same results for $n = 0$ and $n = 1$ were obtained. Despite the same results, solving the problem by combining *Electrostatics* and *Electric Currents* exhibited much longer computation times. For these comparisons, the meshing had to be relatively coarse (*fine Free Tetrahedral* mesh for the u-shapes and *normal Free Tetrahedral* mesh for the remaining geometry) because otherwise the relative error became greater than the relative tolerance.

The u-shaped geometry can also be generated by drawing the U in a working plane, which is then extruded. Another possible arrangement of the u-shapes is illustrated in Fig. 2.10, for which a sweep of the parameter *x_displ* was carried out. The results for the forces, which are acting on the silicon bodies, are summarized in Fig. 2.11. It can be seen that for each distance between the u-shapes there is always a repulsive net force acting on the u-shapes.

2.5 Summary of Simulations and Consequences for Electric Field Microsensor

The simulations in the sections 2.3 and 2.4 have revealed the following characteristics which should be considered in the simulations of the electric field microsensor:

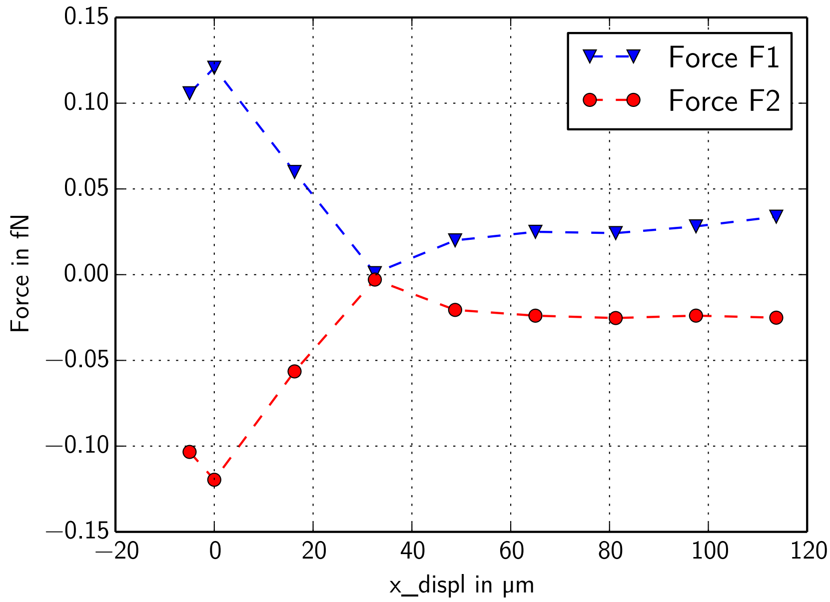

Figure 2.11: Force on two electrically insulated u-shapes for different distances *x_displ*.

- Smaller conducting bodies lead to less electric field distortions but the forces acting on the conductors decrease significantly. In order to maintain a reasonable sensitivity, the geometry of the MEMS transducer should be optimized with regard to maximizing the forces.

- Finer meshing leads to more accurate results but the computation may become much more time-consuming. Therefore, good balance has to be found. Furthermore, the smallest objects in the geometry with the finest mesh elements should be meshed first.

- If the distance between two insulated spheres is small, attractive net forces are exerted on these bodies. For electrically connected spheres, the net force is repulsive. Therefore, multiple transducer units could be included in the electric field microsensor design and cascaded appropriately to increase the total mechanical force.

- For highly symmetric geometries, e.g. two spheres, and for more complex geometries, e.g. two u-shapes, in a constant electric field, the results of the simulations have not shown significant differences between *Electrostatics* and the combination of *Electrostatics* and *Electric Currents*. For the combination *es+ec*, the meshing quality was limited, the computation time was much longer and, still in many cases, the computation found no solutions because of large relative errors. In theory, *Electrostatics* is enough to describe problems where the observation time is much smaller than the charge relaxation time $\tau = \varepsilon/\sigma_{\mathrm{el}}$. The semiconductor silicon, which is the main component of the MEMS transducer, has a charge relaxation time $\tau = 6.6 \cdot 10^{-8}$ s which is almost the average between $\tau = 10^{-19}$ s of the perfect conductor copper and $\tau = 10^{3}$ s of a the good insulator silica glass, in terms of magnitude, so that any of these two approaches can be chosen. In a nutshell, *Electrostatics* should be enough for the COMSOL simulations of the electric field microsensor in an externally applied constant electric field.

3 FEM Based Optimization of Electric Field Sensors

3.1 Characteristics of the First Design

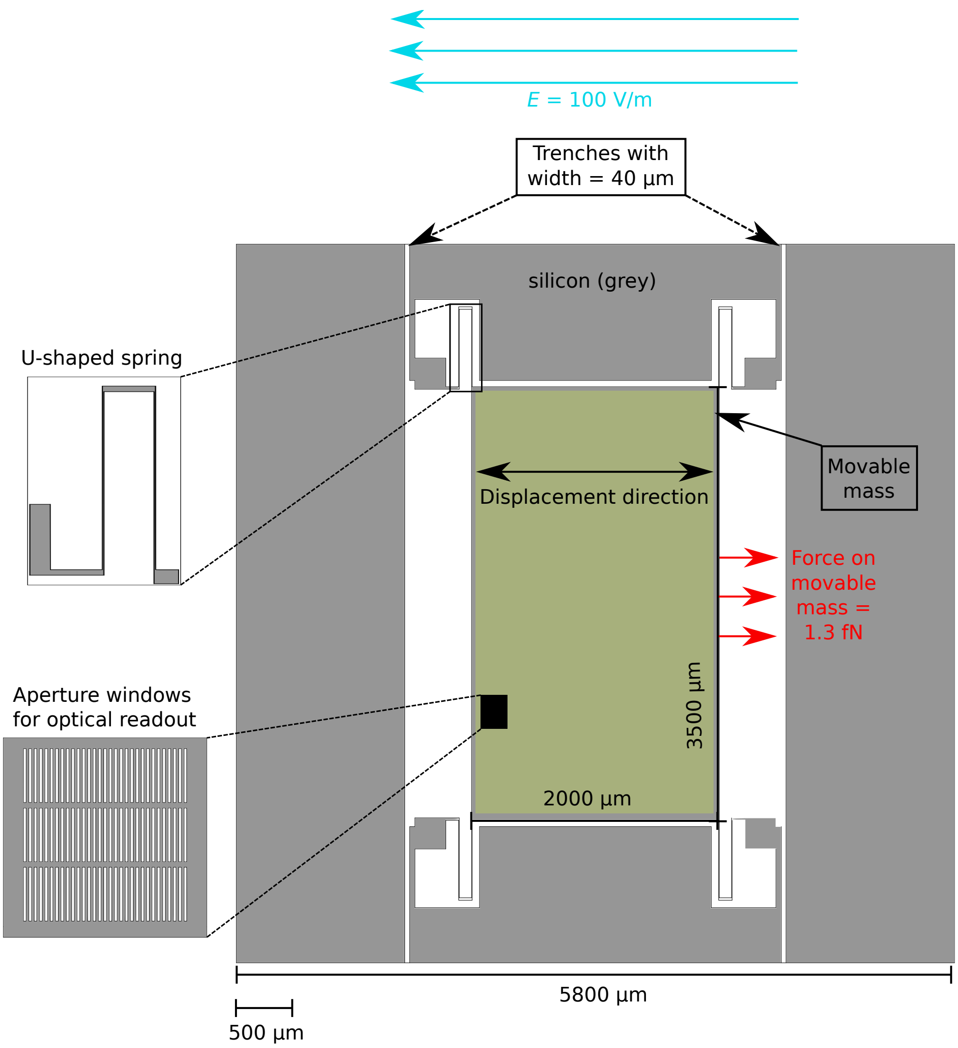

Figure 3.1: Design of the initial silicon device layer for the electric microsensor.

The design of the first movable microstructure for the electro-mechanical transducer is illustrated in Fig. 3.1. The microstructure, also called the movable or proof mass, with

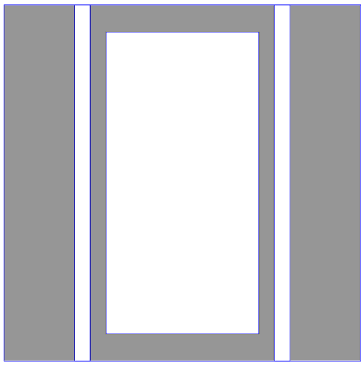

Figure 3.2: Design of the initial handle layer for the electric microsensor.

the aperture holes is located in the center of the chip and connected to the immobile silicon parts via u-shaped springs. Trenches on the left and on the right side of the entire middle silicon domain generate its isolation from the left and the right immobile silicon domains. In section 2.5, it was shown that attractive forces are exerted on two electrically insulated bodies, if the distance between them is small. As a consequence, the seismic mass should be theoretically attracted to the right and to the left immobile silicon domain in an externally applied constant electric field. These electromagnetic forces pointing in opposite directions are equal because of the entirely symmetric geometry which results in minimal forces and bad sensitivity of the MEMS transducer to the electric field.

The relevant parameters for the COMSOL simulation of the silicon device layer with the initial geometry are summarized in Table 3.1. The electric potentials U and $-U$ of the *Block 1* end faces are set to get a constant external electric field of 100 V/m. The device layer is positioned in such a way that the field vectors point in the displacement direction of the movable mass, which is the x-direction. The simulation calculated a rather small force on the movable mass of +1.3 fN acting in positive x-direction.

For the simulation of the complete MEMS chip, the silicon handle layer needs to be added to the geometry: The geometry for a work plane at $z = -10$ μm is again imported from a dxf-file and extruded with a distance of -350 μm from the plane. The initial geometry of the handle layer is illustrated in Fig. 3.2 and basically consists of a closed frame around the movable mass. The spatially separated silicon domains in the handle layer are set on individual floating potentials. The SiO_2 layer, which is sandwiched between the handle and device layer and provides the insulation between them, can be approximated by air for the simulation. Its relatively small thickness of 10 μm yields negligible effects on the electric field and its insulating property for the SOI wafer can be equally described by air. Furthermore, an additional layer with a small thickness would significantly increase the computation time. In theory, the initial handle layer design with a closed frame shields the underside of the device layer from the electric field and the simulation showed that the force on the proof mass decreased by one order of magnitude to -0.4 fN.

Theoretical considerations and FEM simulations have revealed the following drawbacks of the initial design:

Table 3.1: Relevant features for the COMSOL simulation of the silicon device layer with the initial geometry.

Parent node	**Subnode**	**Feature**	**Important feature settings**
Component	Geometry	Work Plane 1	x-y-plane at $z = 0$, import the plane geometry from a dxf-file
Component	Geometry	Extrude	Input object = work plane 1, distance from plane = 45 µm
Component	Geometry	Block 1	Size = (36 mm,36 mm,36 mm), center = (33 mm, 0, 22.5 µm)
Component	Materials	Silicon (single-crystal, isotropic)	Input object = extruded work plane, relative permittivity = 11.7
Component	Materials	Air	Input objects = remaining geometry, relative permittivity = 1
Component	Electrostatics (es)	Floating Potential 1	Boundary selection = boundaries of the right silicon domain
Component	Electrostatics (es)	Floating Potential 2	Boundary selection = boundaries of the middle silicon domain
Component	Electrostatics (es)	Floating Potential 3	Boundary selection = boundaries of the left silicon domain
Component	Electrostatics (es)	Force Calculation 1	Domain selection = movable mass
Component	Mesh	Free Tetrahedral	Input objects = all domains, customized element size parameters are: minimum element size = 1 µm, maximum element size = 36000 µm, maximum element growth rate = 1.5

Table 3.2: Comparison of the simulated forces on the proof mass for the asymmetric device-layer geometry to the forces for the symmetric device-layer geometry.

	Force in fN for symmetric device layer	**Force in fN for asymmetric device layer**
Simulation of device layer	1.3	303.9
Simulation of SOI wafer	-0.4	30.3

- The opposite forces on the movable mass to the right and to the left immobile silicon domains are almost equal due to the entirely symmetric geometry of the silicon device layer.
- A closed frame for the handle layer geometry shields the bottom side of the device layer from the electric field.

3.2 Simulations of Different Electric Field Microsensor Designs

3.2.1 Integration of Asymmetry into Initial Device-Layer Design and Influence of Different Handle-Layer Designs

In order to make the geometry in the device layer asymmetric, the left and the central silicon domains are electrically connected. In the simulation, this can be realized by adding another floating potential for the boundaries of the central and the left silicon domains which are opposite each other. The simulated forces on the proof mass for the asymmetric device-layer geometry compared to the symmetric device-layer geometry are summarized in Table 3.2. The forces for the asymmetric geometry of the device layer are approximately two orders of magnitude larger than the forces for the symmetric geometry. This significant increase confirms that asymmetry should always be included in new device-layer designs.

The electric potential distributions for symmetric and asymmetric device-layer geometries are illustrated in Fig. 3.3 and Fig. 3.4, respectively. The individual silicon domains are on constant potentials, which are determined by the external electric field, and between the domains the electric potential varies. As the left, central and right silicon domains are on separate floating potentials in the symmetric device layer (see Fig. 3.3), the electric potential approximately exhibits the same gradient in positive x-direction as in negative x-direction. In general, the force acting on a conductor surface depends on the local surface charge density because of $\mathbf{E} = -\nabla V$ and $\mathrm{d}\mathbf{F} = \frac{\sigma^2}{2\varepsilon_0}\mathrm{d}A \cdot \hat{\mathbf{n}}$ with the surface charge density σ depending on the local electric field. In this case, the resulting force on the proof mass in the displacement direction should be zero. The electric potential distribution for the asymmetric device-layer is illustrated in Fig. 3.4 and the following characteristics can be noticed: On the one hand, there is almost no variation in the electric potential between the left and central silicon domains as they are on the same floating potential. On the other hand, the gradient of the electric potential in positive x-direction is even greater because the left and central silicon domains, which are now electrically connected, are on a smaller potential than before, while the right silicon domain is on the same floating potential as before. The greater potential difference between these neighbouring silicon domains increases the force on the proof mass in positive x-direction, while the force in negative x-direction is almost zero.

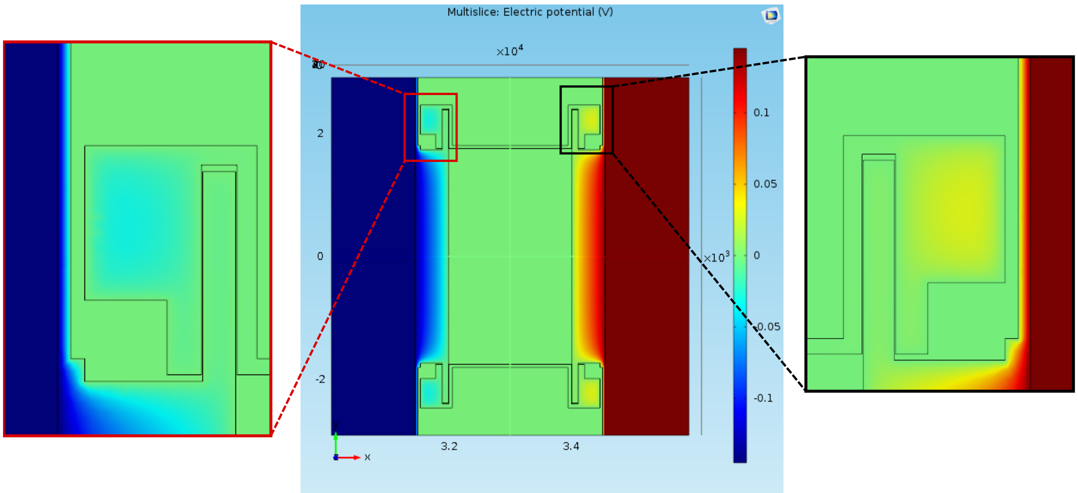

Figure 3.3: Distribution of the electric potential in the x-y-plane for a device layer with symmetric geometry.

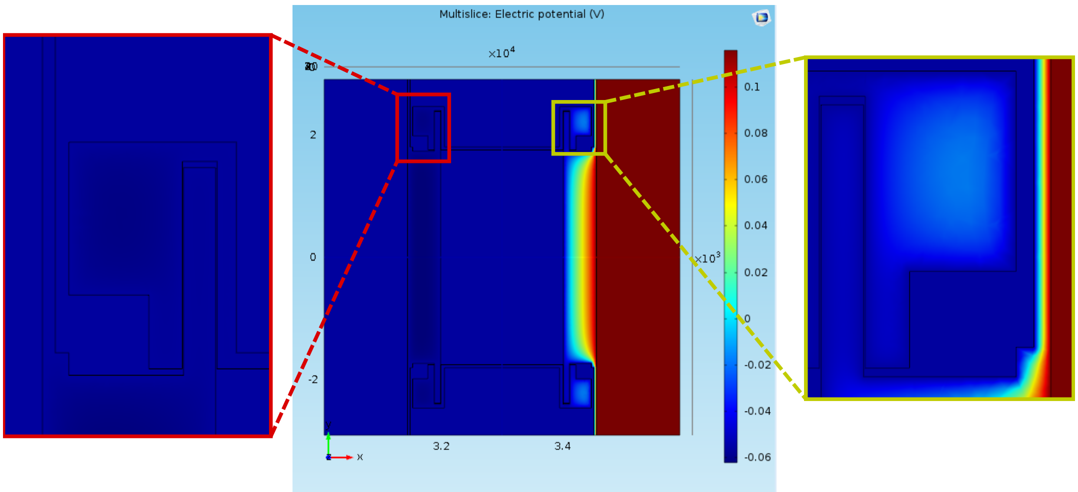

Figure 3.4: Distribution of the electric potential in the x-y-plane for a device layer with asymmetric geometry.

The force on the electric field sensing element of the device layer can also be increased by changing the handle-layer geometry. A frame around the movable mass shields the

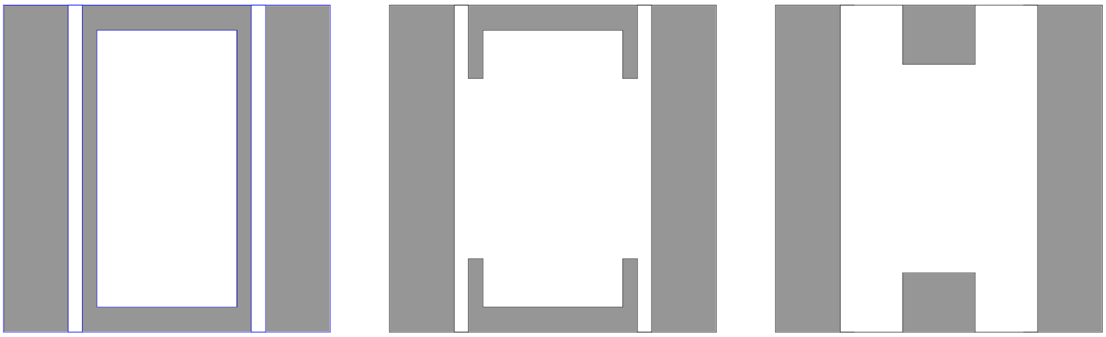

(a) $F = 30.3$ fN. (b) $F = 219.6$ fN. (c) $F = 347.4$ fN.

Figure 3.5: Illustration of different handle-layer geometries. They are simulated in combination with the asymmetric device layer to get the respective forces on the proof mass F. (a) Initial handle layer design. (b) Handle layer design where the vertical connecctions in the frame are cut. (c) Design with small silicon plates for the fixation of the central silicon domain of the device layer.

sensing parts of the device layer from the electric field to a significant extent. In Fig. 3.5a, the initial handle-layer design is illustrated. Fig. 3.5b depicts a possibility to open the frame for reduced shielding increasing the force on the proof mass by a factor of 7. In the handle-layer design illustrated in Fig. 3.5c, the inner parts are reduced to small silicon plates which are necessary for the fixation of the central silicon domain but this increases the force on the movable mass only by a factor of 1.6. Therefore, it is obviously important that the sensing parts of the device-layer are not entirely framed by the handle-layer. Further reductions of silicon in the handle layer do not significantly increase the forces.

3.2.2 Various Device-Layer Designs for Maximizing the Electromagnetic Force on the Proof Mass

Beside the integration of asymmetry into the geometry of the device-layer, there are various possibilities for maximizing the force on the movable mass.

The trenches separating the central immobile silicon from the outer immobile silicon, have a relatively small width of 40 μm. Therefore, a large electric potential gradient is generated in these trenches tat acts on the majority of charges residing in the right silicon domain. As the silicon domains on the left and on the right side of the trenches are immobile, this has no effect on the sensitivity of the proof mass to the electric field. Fig. 3.6 shows the high concentration of charges on the conductor surfaces surrounding the respective trenches. As a consequence, only few charges reside on those surfaces of the movable mass and the right immobile silicon volume which are vis-a-vis to each other. As these *sensing surfaces* mainly determine the electromagnetic force acting on the movable mass, the resulting sensitivity of the proof mass to outer electric fields is insufficient.

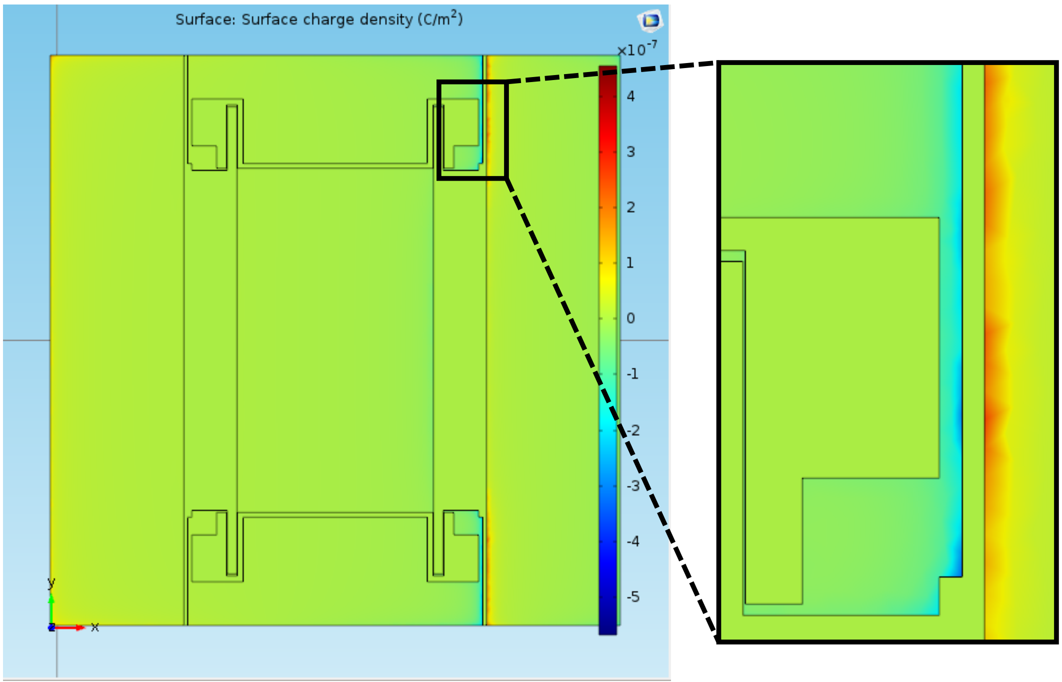

Figure 3.6: Simulated surface charge density on the device layer in an outer electric field of 100 V/m. The left silicon domain is electrically connected to the central silicon domain. The electric field points in negative x-direction.

Fig. 3.7 shows two possibilities to increase the sensitivity of the movable mass by avoiding small distances between the central and the right immobile silicon domains and Fig. 3.8 shows the corresponding surface charge density distributions.

The design in Fig. 3.7a leads to an almost equal distribution of positive charges along the surface of the right silicon domain which is vis-a-vis to the middle silicon domain (see Fig. 3.8a). The negative charges in the middle domain are now concentrated on the sensing surface of the proof mass so that the electromagnetic force on the proof mass is increased by a factor of 3. The absence of trenches, however, provides no protection of the device-layer microstructure against unwanted water penetration during the cutting of the wafer. A compromise with short trenches for reasonable water protection is illustrated in Fig. 3.7b. Fig. 3.8b shows that many charges are again concentrated in the trench regions so that the electromagnetic force on the proof mass only increases by a factor of 2 in comparison to the initial design, where the left and central silicon domains are electrically connected.

The following characteristics can be summarized and are important for further design variations:

- The charges in the silicon domains tend to accumulate on those opposite surfaces which are on different potentials and close to each other.

- The charge densities in the sensing surfaces of movable mass and right silicon domain mainly determine the electromagnetic force acting on the movable mass

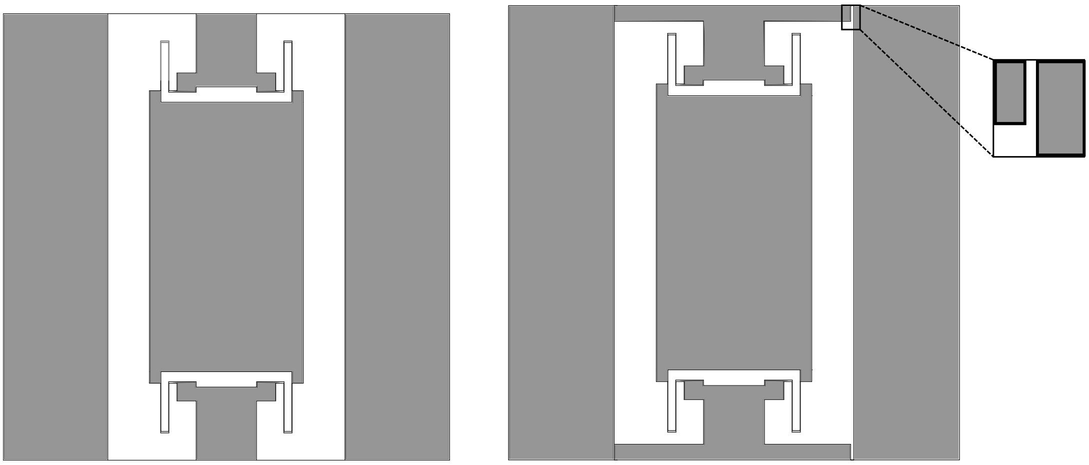

(a) F = 911.1 fN.   (b) F = 678.4 fN.

Figure 3.7: Device-layer designs with (a) maximum distance and (b) short trenches between the central and right immobile silicon domains. In both designs, the central and the left silicon domain are electrically connected, respectively. Only the device-layer is simulated for calculating the force on the proof mass F. The force results should be compared to F = 303.9 fN of the initial design, where the left and central silicon domains are electrically connected.

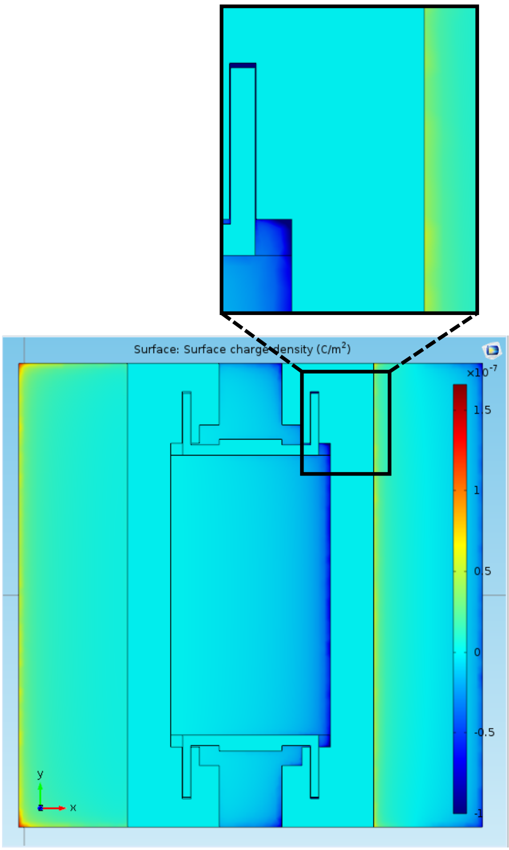

(a) F = 911.1 fN.

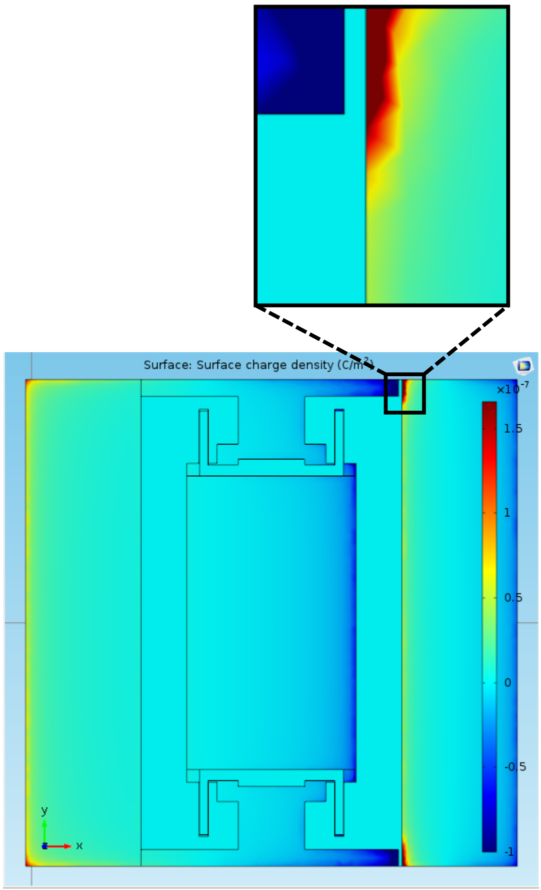

(b) F = 678.4 fN.

Figure 3.8: Plot of the simulated surface charge density for the device-layer design with (a) maximum distance and (b) short trenches between right and central immobile silicon domains. In both cases, the electric field vectors point in negative x-direction.

and, hence, the sensitivity of the electro-mechanical transducer to electric fields.

- The area of the sensing surface of the movable mass should be maximized, while regions with small distances between the central and the right immobile silicon domains should be minimized.
- The distance between the sensing surfaces should be minimized.

Three different device-layer designs considering these characteristics are illustrated in Fig. 3.9 and the respective electric potential distributions are summarized in Fig. 3.10. Here, the movable mass is extended in the positive x-direction until a distance to the right immobile silicon domain of 50 µm.

The design in Fig. 3.9a features air gaps between the middle and the right immobile silicon volumes that are located to the left of the gap between the sensing surfaces (*sensing gap*). The related plot of the electric potential indicates that the electric field is strongly bent in the regions around those air gaps. In this part, forces are exerted on the movable mass, which are not parallel to the displacement direction of the proof mass and, hence, do not contribute to its sensitivity to outer electric fields. In Fig. 3.9b, the air gaps are in one line with the sensing gap and the electric field is less bent which results in a slight increase in force. However, the electric field still enters regions which do not contribute to the sensitivity of the sensor. In the design illustrated in Fig. 3.9c, the movable mass is extended in positive and negative y-direction so that the area of the sensing surface of the movable mass is maximized. Figure 3.10c also indicates that this device-layer design hinders the electric field from entering regions which do not contribute to the sensor's sensitivity. Therefore, the electromagnetic force on the movable mass is increased to 7.3 pN.

With the design in Fig. 3.9a, several widths of the sensing gap from 150 µm down to 3 µm were simulated and the results for the electromagnetic forces on the movable mass are summarized in Fig. 3.11a. It can be seen that the force increases with decreasing distance d and this inverse relationship can be approximately described by $\frac{1}{d}$. For example, the force at a distance of 3 µm is, by a factor of 100, greater than the force at a distance of 150 µm. This relatively large increase emphasizes that the sensing surfaces of the movable mass and right immobile silicon domain should be located as close to each other as possible.

The use of a thicker silicon device layer is another possibility to increase the sensitivity because more charges are present. For the design illustrated in Fig. 3.7b, thicknesses from 45 µm to 360 µm have been simulated and the results for the forces on the proof mass are summarized in Fig. 3.11b. The force increases linearly with increasing thickness. However, the thicker springs will lower the flexibility of the movable mass compensating the increase of the force. The Bosch Deep Reactive Ion Etching to form the microstructures also gets more challenging and the minimal width of the etched trenches in the device layer has to be larger. Therefore, it is better to minimize the sensing gap width down to the µm-range and to keep the device-layer thickness at 45 µm.

The influence of the aperture holes in the proof mass on the electromagnetic forces was also investigated and the results of the simulations are summarized in Table 3.3.

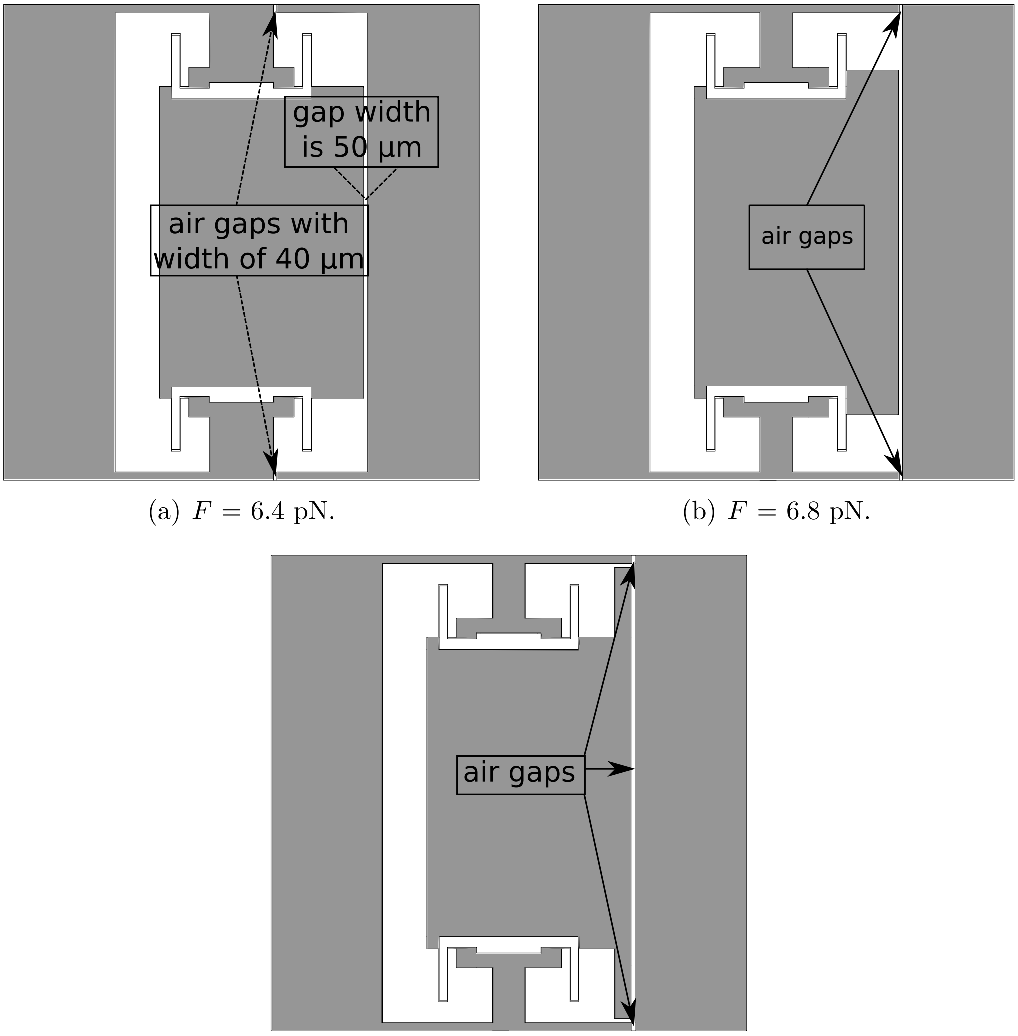

(a) $F = 6.4$ pN. (b) $F = 6.8$ pN. (c) $F = 7.3$ pN.

Figure 3.9: Illustration of device-layer geometries, (a) where the trenches between the central and the right immobile silicon domain are located to the left of the sensing gap, (b) where the trenches are located in one line with the sensing gap, (c) where the trenches are located in one line with the sensing gap and where the movable mass is extended in y-direction. The width of the gap between the sensing surfaces (*sensing gap*) is 50 µm. Only the device layer is simulated to calculate the force on the proof mass F. The force results can be compared to $F = 0.3$ pN of the initial design, where the left and central silicon domains are electrically connected.

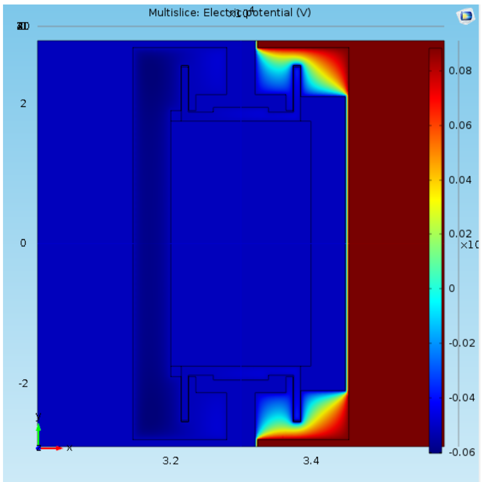

(a)

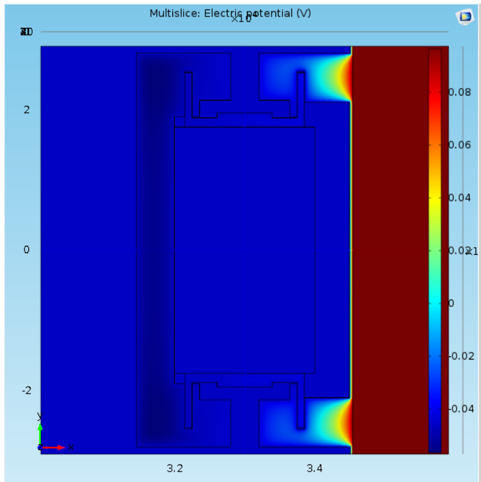

(b)

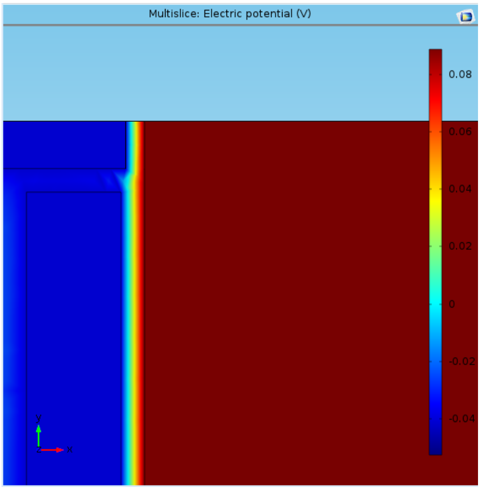

(c)

Figure 3.10: Distribution of the electric potential for the device-layer design illustrated in (a) Fig. 3.9a, (b) Fig. 3.9b and (c) Fig. 3.9c .

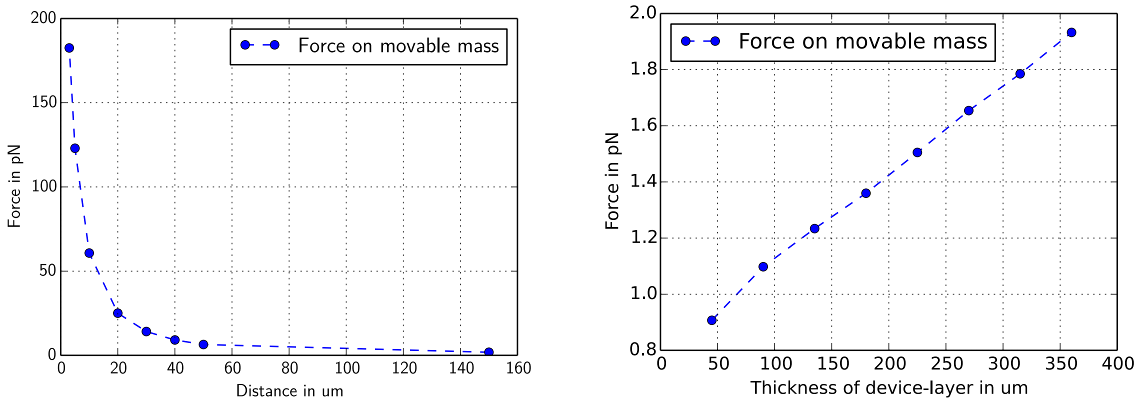

(a) (b)

Figure 3.11: Forces on the movable mass (a) for different distances between the movable mass and the right fixed silicon domain and (b) for different thicknesses of the device-layer. Only the device-layer is simulated.

Table 3.3: Electromagnetic forces on the proof mass F for proof masses with and without a hole in the middle.

Simulated geometry	**F in fN with aperture**	**F in fN without aperture**
Only device layer with symmetric initial geometry	-1.4	1.3
Only device layer with asymmetric initial geometry	289.5	303.9
Initial asymmetric device layer and initial handle layer	20.8	30.3
Initial asymmetric device layer and handle layer from Fig. 3.5b	204.4	219.6

There are only slight differences, which can be traced back to mesh inaccuracies, and the assumption in the previous statement, that the movable mass with its aperture holes can be properly simulated without the holes, still holds. In a static system, the charges in the movable mass are located on its end surfaces so that the semiconductor's surfaces in each window are free from charges. As the electric potential is also approximately constant across one window, no forces are acting on those boundaries.

3.2.3 Various Devices for Improved Water Protection

The fabrication of the first MEMS generation with the device-layer design illustrated in Fig. 3.1 has revealed that water, that was applied for dicing, has partly reached the interior of the MEMS. Closed silicon domains would provide good protection against unwanted water filling but it was shown that silicon frames around the sensing microstructure dramatically decrease the electromagnetic forces. Therefore, a compromise between good water protection and reasonable sensitivity has to be found.

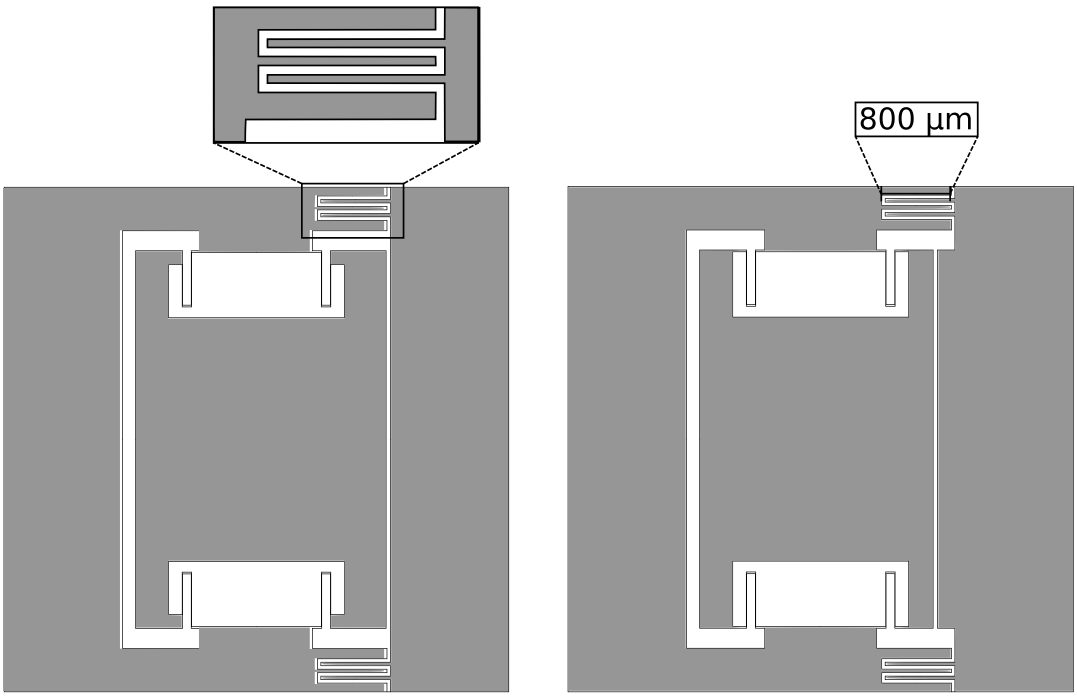

(a) (b)

Figure 3.12: Two designs of the device layer with simulated forces on the proof mass F. The gap between the movable mass and right silicon domain is 50 µm. The force results should be compared to $F = 5.8$ pN of the design without meander. (a) $F = 2.8$ pN. (b) $F = 2.7$ pN.

The introduction of meanders into the channels could increase the fluidic resistance without shielding the interior of the chip entirely from the outer electric field. Fig. 3.12a shows one possibility of meander-shaped channels, where the orientation of the u-springs is also reversed and the movable mass is more symmetric to the center of the chip. In Fig. 3.12, the proof mass has been changed in such a way that the u-springs are symmetric to the x-direction which minimizes nonlinear terms in the excitation of the springs. Furthermore, the immobile silicon domains at the edges of the chip are thicker than in Fig. 3.9 for better stability of the device layer. Otherwise, small silicon edges could break easily even under small pressures. These slightly thicker silicon edges lead to a decrease in the force on the proof mass from 7.3 pN to 5.8 pN. From now on, this basic structure of the mass with its u-springs and the thicker silicon edges basically stays the same for the next design variations. The meanders with lengths of 800 µm should represent an obstacle for the water flow. In Fig. 3.12b, there is a bend in the right silicon domain so that water flow coming out of the meander-shaped channels does not go directly into the sensing gap but is partly blocked by this corner. The slight shielding

Table 3.4: Force on the proof mass for different meander locations relative to the gap between movable mass and right silicon domain (sensing gap). Only the silicon device is simulated. The basic structure of the device layer is illustrated in Fig. 3.12.

Side of meanders to sensing gap	**Number of horizontal channels**	**Length of horizontal channel in μm**	**Force in pN**
left	2	400	4.8
left	2	800	3.9
left	4	400	4.0
left	4	800	2.8
right	2	400	4.8
right	2	800	3.8
right	4	400	4.0
right	4	800	2.7
middle	4	400 and 200	4.5
middle	4	800 and 400	3.3

influence of the meanders leads to a decrease of the electromagnetic force on the proof mass by a factor of approximately 2.

Various locations of the meanders have been simulated and the result for the electromagnetic forces are summarized in Table 3.4. Obviously, the location of the meanders on the left side of the sensing gap generates the largest electromagnetic forces. This location of the meanders, which can be seen in Fig. 3.12, is used for the following simulations, although there are only small differences between the various meander locations. Another consequence of Table 3.4 is that the force decreases with increasing length of the horizontal meander channels, but only to a small extent. Longer meanders could improve the fluidic resistance of the channels against unwanted water filling.

It was already shown in Fig. 3.11 that in the case of no meanders, the electromagnetic forces increase with decreasing sensing gap width. As a consequence of the simulated forces summarized in Table 3.5, this increase is the same, if not even larger for device layers with meanders. This leads to the conclusion that meander-shaped channels have no negative effects on the force for decreasing sensing gap widths. Therefore, slightly smaller forces on the proof mass can be compensated to a significant extent by decreasing the sensing gap width.

An additional channel with a "reservoir" at its end, which is illustrated in Fig. 3.13a, could improve the water protection of the movable elements, i.e. springs and proof mass, against unwanted water filling during the cutting of the wafer. The water flow is divided into two parts where one goes into the reservoir via the first channel and the other one to the proof mass via the second channel. The diameter of the first and second channel are chosen to be 40 μm and 50 μm, respectively.

As the surfaces that enclose these additional channels are on the same potential, the

Table 3.5: Electromagnetic forces on the proof mass F for different gap widths d are compared between device layers with and without meanders. Only the device layer is simulated.

d in µm	F relative to $F = 7.3$ pN at $d = 50$ µm without meanders (see Fig. 3.9c)	F relative to $F = 2.8$ pN at $d = 50$ µm with meanders (see Fig. 3.12a)	F relative to $F = 2.7$ pN at $d = 50$ µm with meanders and additional corners (see Fig. 3.12b)
10	8.3	11.4	14.9
5	16.7	25.9	33.8
3	24.8	41.4	54.2

electric field does not enter these regions which can be seen in Fig. 3.13b. Therefore, the additional channels have no influence on the electromagnetic forces. Simulations have proven that the size of the reservoirs and the length of their connecting channels do not change the forces on the movable mass significantly. The variations are so small that they can be traced back to mesh inaccuracies. The force for this design $F = 3.0$ pN is larger than the force for the similar design illustrated in Fig. 3.12b because the movable mass is extended in positive and negative y-direction in order to increase the area of the sensing surface of the proof mass.

In Fig. 3.5, several handle-layer designs have already been introduced and simulations have shown the importance that the sensing parts of the device layer are not entirely framed by the handle layer. Furthermore, the enlargement of openings in the handle layer frame has no relevant influence. Figure 3.14a illustrates the basic geometry for the handle layer being used for the subsequent simulations. The small openings with a width of 250 µm only lead to a minor decrease in the force from 3.0 pN to 2.3 pN and the handle layer should still represent some water protection of the movable elements in the device layer. The respective potential distributions show that the electric field does not enter all bottom regions of the device layer through the handle layer. As a consequence of the electric potential plot in Fig. 3.14c, it does, however, enter those parts where proof mass and right silicon domain of the device layer are vis-a-vis to each other and where the force on the movable mass is mainly determined. At the top-side of the handle-layer, the electric field is then confined to the sensing gap in the device layer which can be seen in Fig. 3.14b. The simulation of the entire SOI wafer requires an additional layer between the device and handle layer representing the 10 µm thick buried SiO_2 for making the meshing possible. At first, the device layer with the spring's width of 4 µm as the minimum mesh element size is meshed. The other domains are meshed in the following order: the additional layer in the regions beneath the sensing gap with a minimum element size of 100 µm, the remaining additional layer with normal element sizes, the handle layer beneath the sensing gap with a minimum element size of 100 µm, the remaining handle layer and, in the end, the remaining geometry with normal mesh element sizes. For all domains, the 3D *Free Tetrahedral* mesh is carried

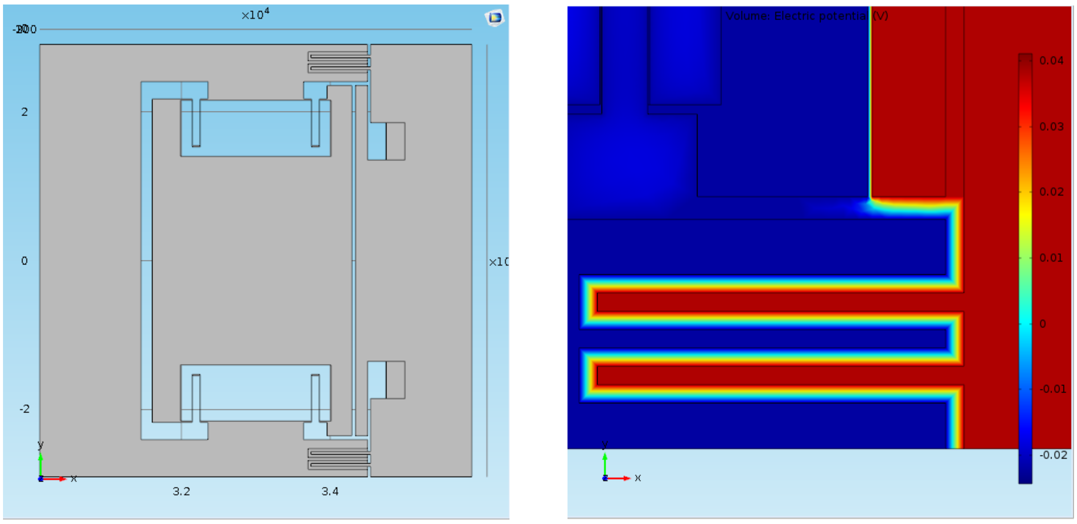

(a) (b)

Figure 3.13: (a) Illustration of the MEMS transducer with meanders and reservoirs from the top side. The simulated force F of 3.0 pN should be compared to $F = 3.0$ pN of the same geometry without the reservoirs and their connecting channels. (b) Simulated electric potential zoomed to the lower meander-shaped channel. The sensing gap width d is 50 µm. Only the device layer is simulated.

out. Especially these mesh settings allow to simulate the important regions near the sensing gap and meanders very accurately within a few minutes.

3.2.4 Simulation of Chrome Apertures

After the fabrication of the SOI wafer, a glass wafer holding a chrome aperture array, is bonded onto the top side of the SOI wafer. Although the chrome layer is approximately 100 nm thick, it has an influence on the electric field sensing elements of the device layer, due to its high conductivity. Shielding effects may lower the sensitivity of the movable mass to electric fields.

For the small thickness of the chrome layer in the submicrometer range, the physics interface *Electric Currents, Shell* needs to be added to the study. This interface models steady electric currents in thin current-conducting shells and solves for the electric potential. It considers extremely thin domains as boundaries with specific thicknesses instead of volumes and, hence, enables the meshing of such geometries. The physics *Electrostatics* (*es*) and *Electric Currents, Shell* (*ecs*) are coupled by setting the electric potential of *ec* equal to the electric potential of *ecs* on the boundaries of the chrome layer.

In the initial design, the entire glass wafer is covered by chrome except for an array of rectangles. As the chrome layer is on one potential, the potentials of the surfaces enclosing one aperture window are equal resulting in an almost constant electric potential

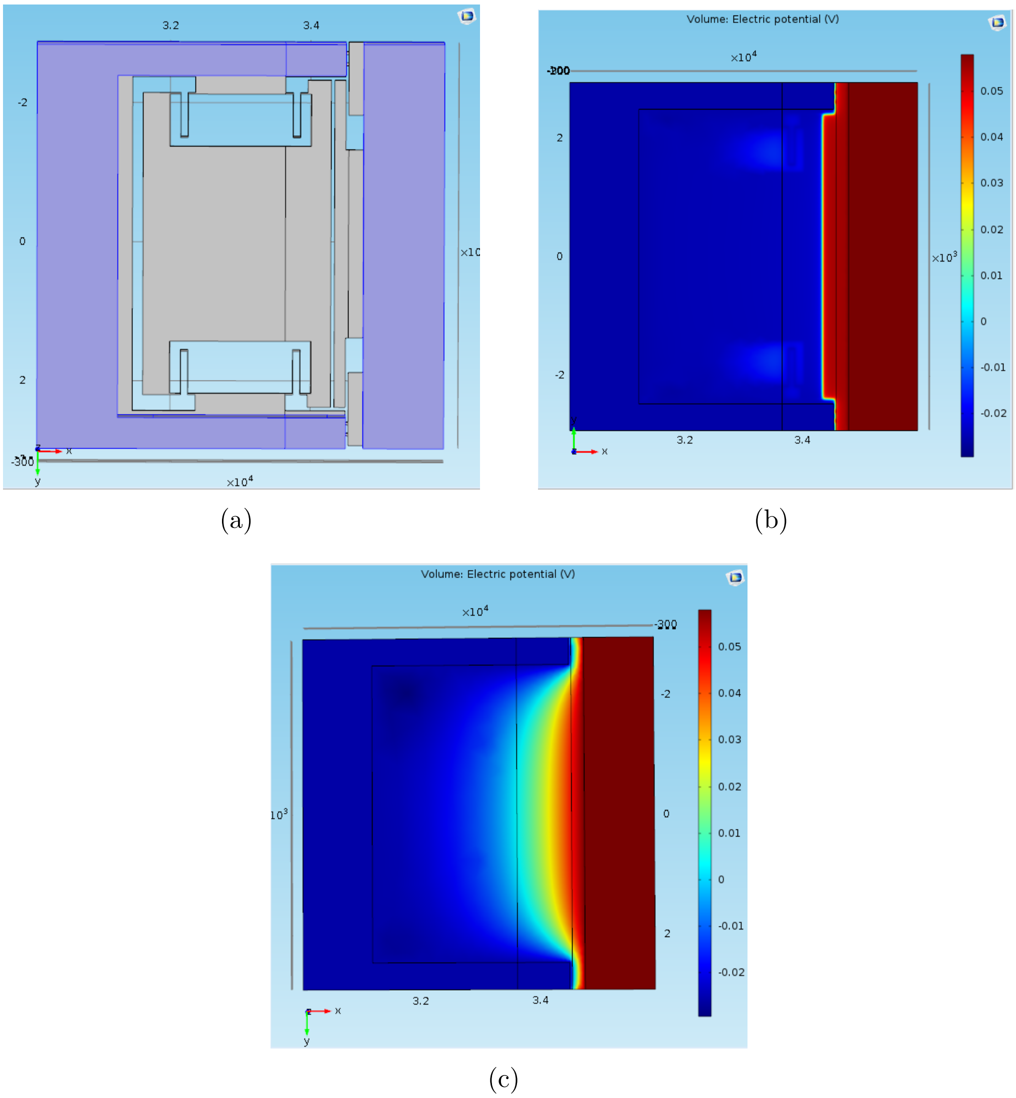

Figure 3.14: (a) Illustration of the MEMS transducer with the final handle layer (in light blue) from the bottom-side. The grey domains are the device layer. The device layer (see Fig. 3.13a) and handle layer are both simulated and the force on the proof mass $F = 2.3$ pN is calculated. This force should be compared to $F = 3.0$ pN where only the same device layer with meanders and reservoirs was simulated. (b) Plot of the electric potential for the top side of the handle layer. (c) Electric potential distribution for the bottom side of the handle layer.

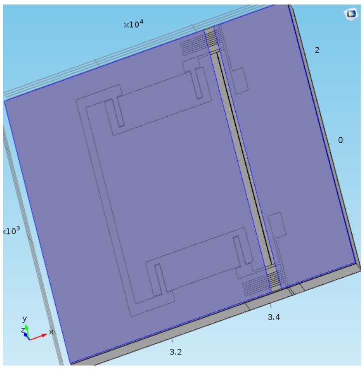

(a) $F = 1.6$ pN.

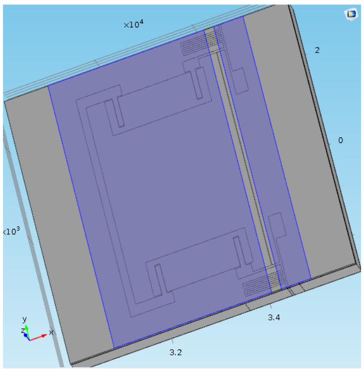

(b) $F = 0.8$ pN.

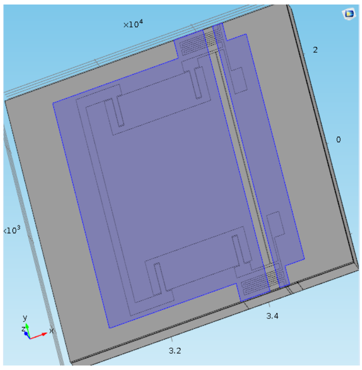

(c) $F = 2.2$ pN.

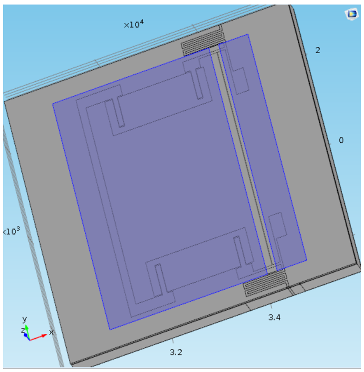

(d) $F = 5.4$ pN.

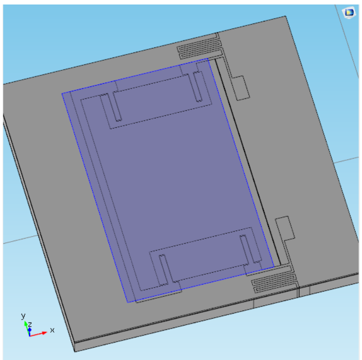

(e) $F = 25.0$ pN.

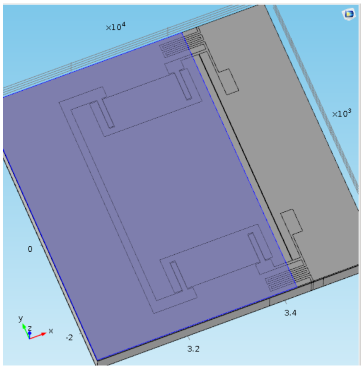

(f) $F = 16.3$ pN.

Figure 3.15: Designs of various chrome layers. The entire SOI wafer, consisting of the device layer from Fig. 3.16b and the handle layer from Fig. 3.14a, in combination with the chrome layer on top of it is simulated. The simulated forces on the proof mass F should be compared to $F = 35.2$ pN of the simulation of this SOI wafer without the chrome layer. The width of the gap between proof mass and right silicon domain in the device layer is 10 µm. The initial chrome layer design, which entirely covers the device layer, significantly decreases the force on the proof mass to $F = 0.05$ pN.

Table 3.6: Electromagnetic forces on the proof mass F for different gap widths. The final device layers, illustrated in Fig. 3.16, are simulated in combination with the handle layer from Fig. 3.14, respectively.

d in µm	F in pN without meanders	F in pN with meanders
10	74.1	35.2
5	132.7	79.0
3	254.7	123.1

across the window. In theory, the electric field can not pass the chrome layer through the aperture holes so that the chrome layer can generally be simulated without any holes. In Fig. 3.15, various chrome layers are illustrated with their respective electromagnetic forces on the proof mass. The initial chrome layer design decreases the force by almost 3 orders of magnitude and obviously shields the top side of the device layer from the electric field to a significant extent. If the sensing gap is not covered by chrome, the force only decreases by a factor of approximately 20. The simulations have shown that the chrome layer should cover the device layer either on the left or on the right side of the sensing gap. If the trenches in the device layer are not covered partly by chrome, the light flux going through the device layer for the optical readout of the mechanical deflection does not only pass the windows of the aperture array but it also goes through the trenches. This constant background light would decrease the sensitivity of the microsensor to electric fields. The chrome layer designs illustrated in Fig. 3.15e and 3.15f should represent a good balance between large forces on the proof mass and good shading of the trenches in the device layer.

3.3 Final Device, Handle and Chrome Layer Designs

Now, the most important findings of the simulations can be considered to design device, handle and chrome layers for maximum electromagnetic forces on the proof mass. In spite of some minor changes, these final designs basically remain during the implementation of the geometries into the Python code for drawing the lithography masks.

Fig. 3.16 presents the final device layer designs for maximum forces on the proof mass without and with emphasis on the water protection of the sensing elements. The gap between the proof mass and the right immobile silicon domain should be as small as possible and simulations of the final device layers in combination with the handle layer, which are summarized in Table 3.6, have, once again shown the significant force increase for decreasing distance. The minimum gap width that can be etched into the 45 µm thick silicon device layer with the Bosch DRIE is 3 µm. In this case, the force on the proof mass increases to 254.7 pN without meanders and to 123.1 pN with meanders resulting in very good sensitivities to the electric field. However, such small structures are more prone to failure so that gap widths of 5 µm, 10 µm and 20 µm, which exhibit also reasonable sensitivities, will be applied instead.

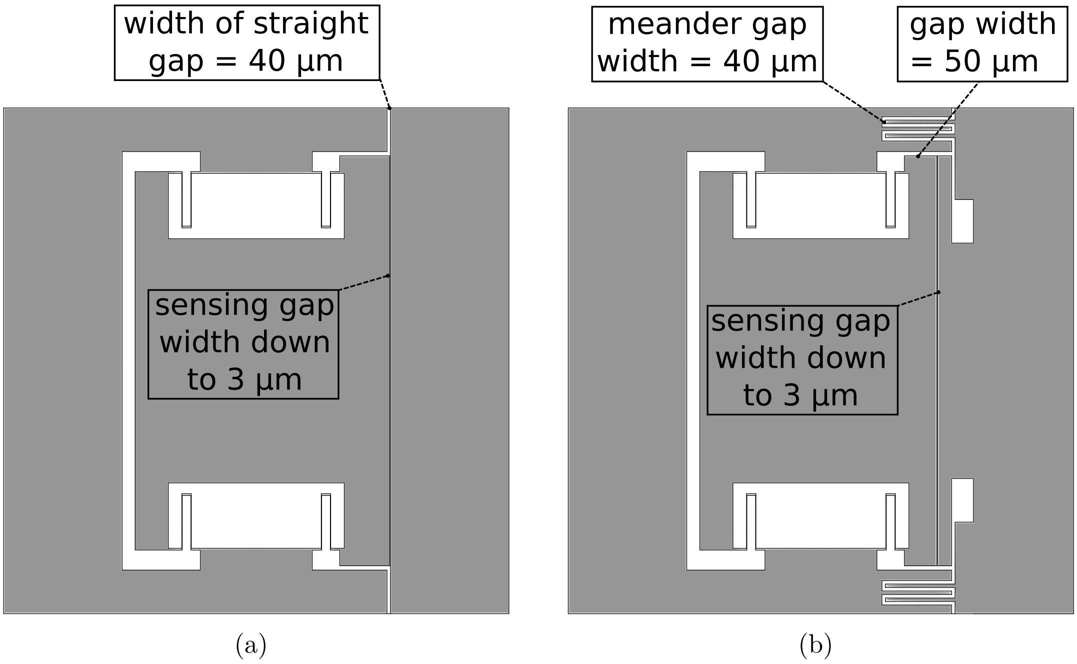

Figure 3.16: Illustration of the final designs for (a) maximum electromagnetic force on the proof mass and (b) good water protection of the movable elements against unwanted water filling during the wafer cutting. The handle layer from Fig. 3.14a in combination with these device layers is simulated and the force on the proof mass F is calculated.

(a) Final handle layer (grey) for maximum force on proof mass.

(b) Final handle layer (grey) for good water protection.

Figure 3.17: Illustration of the final handle layer designs for (a) maximum electromagnetic forces and (b) good water protection of the movable elements against unwanted water filling during the wafer cutting.

The device layer design with emphasis on maximum electromagnetic forces is combined with the final handle layer design illustrated in Fig. 3.17a, while the device layer with emphasis on water protection is combined with the handle layer from Fig. 3.17b.

Another possibility to prevent the water from filling the microstructure in the device layer are blocking elements in the channels. Device and handle layers are taken from Fig. 3.16a and 3.17a, respectively. In the device layer, two 5 μm thick blocking elements are included in the gap between the left immobile and the right immobile silicon domains and in the handle layer, two 5 μm thick blocking elements are placed in the gaps between the left and right silicon domains. After the fabrictation of the chip, these additional elements need to be eliminated because otherwise, the interior of the chip would be entirely shielded from the outer electric field. For this, the two bondpads, which were deposited onto the silicon device in the fabrication, are connected to electrodes and a relatively large voltage is applied. As one bondpad is located on the left silicon domain and the other on the right silicon domain, a high potential difference between these two domains occurs resulting in large current densities in the blocking elements. They are partly removed by Joule heating and the electric connection between the left and the right silicon elements is broken up.

4 Summary and Outlook

4.1 Summary of FEM Simulations

As a result of the previous simulations, the most important findings of the device layer for new designs are:

- Asymmetry needs to be included in the geometry.
- The charges in the silicon domains tend to accumulate on those opposite surfaces which are on different potentials and close to each other.
- The area of the surface of the movable mass, which is vis-a-vis to the right immobile silicon domain, should be maximized and the distance between these surfaces should be minimized.
- Narrow gaps between immobile parts of the middle and the right silicon domains should be minimized.
- Regions, which do not contribute to the sensitivity to electric fields, should be shielded from the outer electric field in order to avoid additional bending of the electric field.
- While the force on the proof mass increases linearly with the device layer thickness, it rises with decreasing width of the gap between proof mass and right silicon domain d. This relationship can be approximated by $\frac{1}{d}$.
- The aperture holes in the device layer have no influence on the electromagnetic forces.
- Meander-shaped channels for better water protection of the sensing elements decrease the force on the proof mass only by a factor of approximately 2. Hence, reasonable sensitivity is maintained.
- The inverse relationship between force on proof mass and sening gap width, which can be approximated by $\frac{1}{d}$, is also valid for device layers with meanders.
- If surfaces that form a channel are on the same potential, the electric field does not enter the channel.
- Additional channels and reservoirs for better water protection can be added to the meander-shaped channels without an influence on the electric field.

The most important characteristics of the handle layer for new designs are:

- The sensing parts of the device layer should not be entirely framed by the silicon domains of the handle layer. This would dramatically decrease the electromagnetic force on the proof mass.
- Small openings in the silicon frame of the handle layer are enough for reasonable sensitivities. Further enlargements of the openings do not significantly increase the forces.
- The openings should be located somewhere beneath the sensing gap so that the electric field can reach the bottom side of the device layer in those regions.

The most important characteristics of the chrome layer for new designs are:

- The electric field can not pass the chrome layer through the aperture windows. If the entire top side of the device layer is covered by chrome, the force on the proof mass decreases by a factor of approximately 1000.
- If the device layer except for the sensing gap is covered by chrome, the force only decreases by a factor of about 20.
- If the chrome layer covers the device layer only on the left side of the sensing gap, the force is reduced by a factor of approximately 2.

4.2 Overview of Fabricated Chip Designs

The following device-layer and handle-layer geometries have been fabricated:

- Device layer with straight trenches between the immobile silicon parts for large electromagnetic forces on the proof mass and reasonable water protection (see Fig. 3.16a). This design is combined with a handle layer containing straight trenches (see Fig. 3.17a).
- Device layer with meander-shaped trenches for better water protection (see Fig. 3.16b) in combination with a handle layer containing meander-shaped channels (see Fig. 3.17b).
- Device layer with straight trenches including a very thin blocking element for water protection during the cutting of the wafer. A handle layer which also contains straight channels and blocking elements, is combined with this device layer. Afterwards the blocking elements should be etched away via high voltages between the left and right silicon domains.

Variable parameters are the stiffness of the spring ($k = 3.5$ for a resonance frequence of the movable mass $f_R = 400$ Hz, $k = 13.5$ for $f_R = 800$ Hz) and the sensing gap width (5 μm, 10 μm, 15 μm).

The fabricated chrome apertures are illustrated in Fig. 3.15a and Fig. 3.15e.

4.3 Problems of Fabricated Chip Designs

The gold leads, which are intended as markers for sawing, should not overlie parts of the channels between the left and right immobile silicon domain. An example for this unwanted electric connection is illustrated in Fig. 4.1, where 300 µm thick blades had to be applied to break up the connection. In general, channels for insulation between the left and right silicon domain should be located in such a way that they do not interfere with the leads after dicing the wafer.

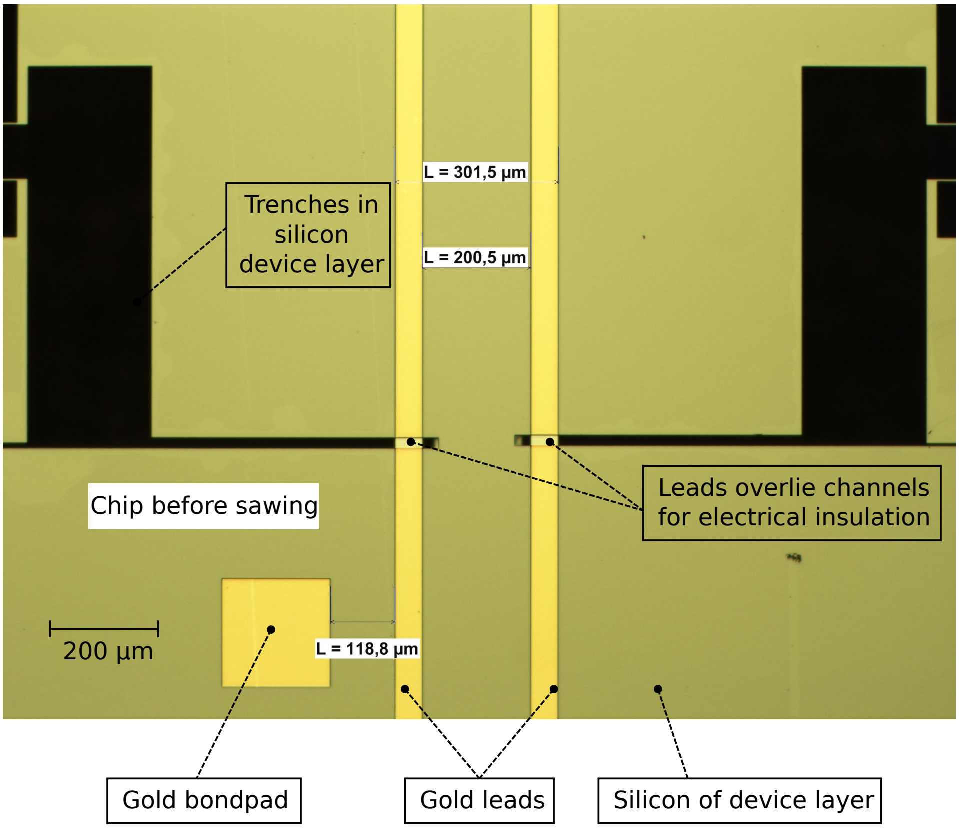

Figure 4.1: Top side of the device layer before the dicing. The gold leads overlie parts of the insulation channels and, hence, lead to an unwanted electric connection between the respective silicon domains in the device layer.

Furthermore, the mask for the SU-8 pattern on the glass wafer should be set in such a way that regions with the movable elements, i.e. the springs and the proof mass, are not touched by SU-8 during the bonding process. An example for an immobilization of the proof mass due to SU-8 is visualized in Fig. 4.2.

The gap width of the channels between the central and the right immobile silicon domains was set to 20 µm to increase the fluidic resistance of the channels. Scanning electron micrographs of the trenches after dicing the chip (see Fig. 4.3) reveal that the trenches are filled with silicon microparticles. During sawing, some of the formed silicon microparticles move into these adjacent trenches and partly obstruct them. Especially

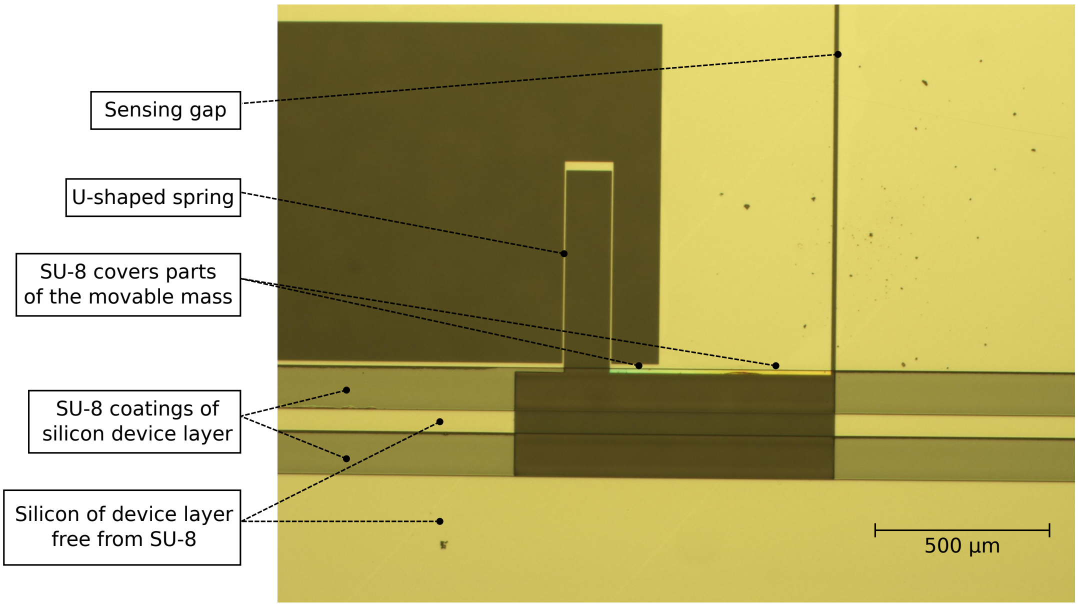

Figure 4.2: Top side of the device layer. The bonding promoter SU-8 cover parts of the movable mass leading to its immobilization.

the trenches in the device layer with a gap width of 20 µm are filled with these particles. As this leads to an unwanted electric connection between the silicon domains of the device layer, the thickness of the trenches between the immobile silicon domains needs to be increased. Figure 4.3 shows that the 150 µm wide gap in handle layer is enough to avoid electric connection due to silicon microparticles. Furthermore, the obstruction of the trenches partly prevents the water from filling the interior of the chip. Therefore, it can not be determined whether the meanders decrease the risk of water penetration.

4.4 Outlook

The expected electrostatic force on the MEMS transducer and, hence, its displacement is relatively small so that other causes, e.g. acoustically induced vibrations, have a large influence on the output signal. To suppress such interferences, the linear displacement transducer could be replaced by a design featuring torsional MEMS excitation which is schematically illustrated in Fig. 4.4.

A differential measurement method can also lead to a further reduction of noise caused by vibrations. For example, two structures from Fig. 4.4 could be located next to each other. While both of them are sensitive to acoustical vibrations, only one is sensitive to the electric field. As a result, the light flux difference compensates the deflections stemming from acoustical vibrations. The important characteristics for maximum sensitivity to electric fields, which have been found in the simulations and are summarized in section 4.1, are still valid for new designs, such as the one featuring torsional excitation. The influence of other interferences like self-charging, contamination or wetting on the accuracy, sensitivity and response of the MEMS transducer should also be considered

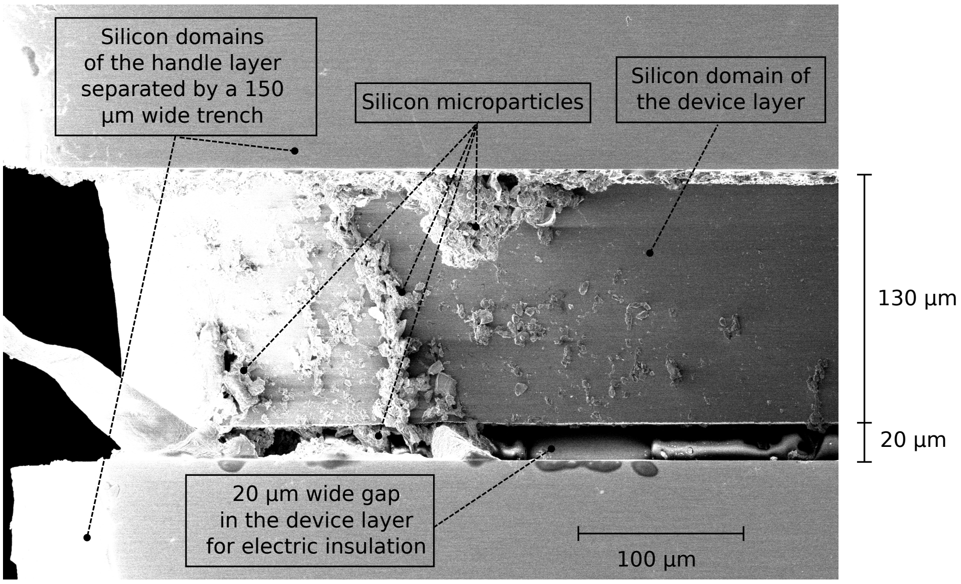

Figure 4.3: Scanning electron micrograph of the bottom side of the MEMS transducer zoomed to gaps in the handle and device layers. The silicon microparticles are residuals from the BOSCH DRIE process and partly remain in the trenches.

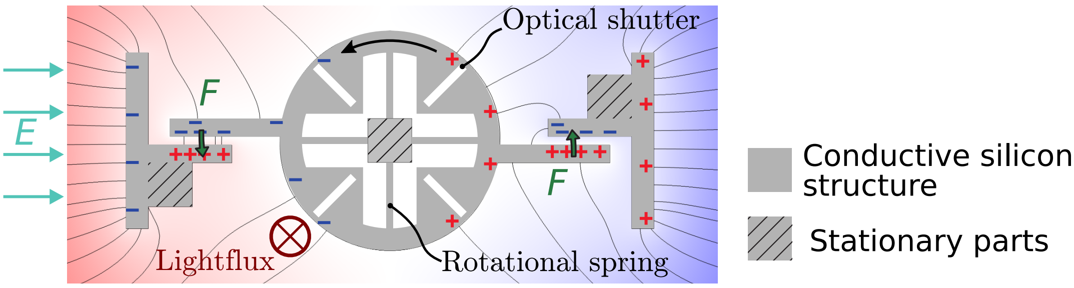

Figure 4.4: Proposal of a rotational electric field microsensor design. The electrostatic forces lead to a torsional deflection of the optical shutter so that the influence of vibrations in the lateral direction is reduced [1].

during the next simulations and experiments.

The displacement of the movable mass depends, amongst others, on the stiffness of the springs, which connect the proof mass to the immobile silicon benches. Decreasing the stiffness leads to larger displacements. However, in general, the displacements should not be too large since otherwise the movable mass may collide with the right immobile silicon domain resulting in failure of the chip. Electro-mechanical simulations and experiments of the chip in an outer electric field should help to find a compromise between large displacements and minimal risk of failure.

It was found that the silicon of the handle layer has an electrical resistance which is by a factor of 10 larger than the electrical resistance of the device-layer's silicon. So, the shielding effect of a handle-layer design with a closed frame around the movable microstructures could be less than predicted. Such a handle layer design does not only reduce the water penetration, but it is also less prone to failure due to fabrication than handle layer designs with meanders. The problem of water penetration during fabrication can not only be addressed by re-designing the MEMS transducer, but also by changing the fabrication process. LASER cutting of the wafer does not require any water rinsing and, hence, represents a convenient alternative for the dicing of the chips.

After re-designing the electro-mechanical transducer design, the optical readout including the micro-opto-electro-mechanical systems (MOEMS) light flux modulator, the glass fibers, collimators, LED and photodiode or phototransistor needs to be implemented. These and further open scientific challenges need to be investigated and solved to produce a sensor which will represent a quantum leap of usability improvement in electric field quantification. State-of-the-art E-field sensors are hardly used in many areas like biology and medicine due to their bulky and complex mechanical configurations. Mobile and precise E-field sensors can not only trigger new science applications in these areas, but also facilitate current applications of E-field sensors, e.g. in the quantification of the atmospheric electric field for early thunderstorm warning and lightning research.

Bibliography

[1] W. Hortschitz. Proposal electric field sensing, February 2015.

[2] E. Williams and E. Mareev. Recent progress on the global electrical circuit. *Atmospheric Research*, 135-136:208–227, Jan. 2014.

[3] NASA. Ionosphere. http://www.hq.nasa.gov/iwgsdi/Ionosphere.html, 1996.

[4] E. Pierce. Atmospheric electricity-some themes. *Bulletin of American Meteorological Society*, 55:1186–114, 1974.

[5] M. Makino M. Takeda, M. Yamauchi and T. Owada. Initial effect of the fukushima accident on atmospheric electricity. *Geophysical Research Letters*, 38(15):1–4, 2011.

[6] C. Shafai A. Roncin and D. Swatek. Electric field sensor using electrostatic force deflection of a micro-spring supported membrane. *Sensors and Actuators A: Physical*, 123-124:179–184, September 2005.

[7] H. Kirkham. On the measurement of stationary electric field in air. In *Conf. on Precision Electromagnetic Measurements*, 2002.

[8] C. Shafai B. Bahreyni, G. Wijeweera and A. Rajapakse. Analysis and design of a micromachined electric-field sensor. *Journal of Microelectromechanical Systems*, 17(1):31–36, 2008.

[9] H. Tao C. Ye Q. Bai S. Chen X. Chen, C. Peng and S. Xia. Thermally driven microelectrostatic fieldmeter. *Sensors and Actuators A: Physical*, 132:677–682, November 2006.

[10] C. Peng X. Chen and S. Xia. Design of a thermally driven resonant miniature electric field sensor with feedback control. In IEEE, editor, *Nano/Micro Engineered and Molecular Sys., NEMS 2008. 3rd IEEE Int. Conf. on*, page 253–256, 2008.

[11] J. Kuang T. A. Denison, J.S. Shafran. A self-resonant memsbased electrometer. In IEEE, editor, *IMTC 2007 - IEEE Instrumentation and Measurement Tech. Conf.*, pages 1–5, May 2007.

[12] N. M. Horenstein and P. R. Stone. A micro-aperture electrostatic field mill based on mems technology. *Journal of Electrostatics*, 51-52:515–521, May 2001.

[13] S. Redlich D. Kalinowski and D. Jager. Novel micromachined fiber-optic e-field sensor. In IEEE, editor, *LEOS'99. IEEE Lasers and Electro-Optics Society 1999 12th Annual Meeting*, volume 1, pages 385–386, 1999.

[14] K. J. Rambo G. H. Schnetzer M. Miki, V. A. Rakov and M. A. Uman. Electric fields near triggered lightning channels measured with pockels sensors. *Journal of Geophysical Research: Atmospheres*, 107(D16):ACL 2–1–ACL 2–11, 2002.

[15] S. Etzel A. Rose and K. Rochford. Optical fiber current sensors in high electric field environments. *Journal of Lightwave Technology*, 17:1042–1048, June 1999.

[16] B. Niu R. Zeng, B. Wang and Z. Yu. Development and application of integrated optical sensors for intense e-field measurement. *Sensors*, 12:11406–11434, August 2012.

[17] H. Brändle K. Bohnert, P. Gabus and A. Khan. Fiber-optic current and voltage sensors for high-voltage substations. In *Proc. of the 16th Int. Conf. on Optical Fiber Sensors, Nara, Japan*, pages 13–17, 2003.

[18] F. Kohl M. Stifter H. Steiner F. Keplinger T. Sauter W. Hortschitz, A. Kainz and J. Schalko. Moems vibration sensor for advanced low-frequency applications with pm resolution. In *EUROSENSORS 2014, the XXVIII edition of the conference series, Brescia, Italy*, 2014.

[19] COMSOL. *COMSOL Multphysics User's Guide*. COMSOL, May 2012.

[20] COMSOL. *Introduction to COMSOL Multphysics*, chapter COMSOL Desktop, pages 14–18. COMSOL, comsol 5.1 edition, 2015.

[21] COMSOL. *Introduction to COMSOL Multphysics*, chapter COMSOL Desktop, pages 18–21. COMSOL, comsol 5.1 edition, 2015.

[22] COMSOL. *COMSOL Multphysics User's Guide*, chapter Meshing, pages 940–941. COMSOL, May 2012.

[23] COMSOL. *COMSOL Multphysics User's Guide*, chapter Solver Studies and Study Types, pages 980–981. COMSOL, May 2012.

[24] D. R. Stump G. L. Pollak. *Electromagnetism*. Addison Wesley, 2002.

[25] D. R. Stump G. L. Pollak. *Electromagnetism*, chapter Basic Principles of Electrostatics, pages 44–49, 65–69. Addison Wesley, 2002.

[26] D. R. Stump G. L. Pollak. *Electromagnetism*, chapter Electrostatics and Conductors, pages 92–96. Addison Wesley, 2002.

[27] D. R. Stump G. L. Pollak. *Electromagnetism*, chapter Electrostatics and Conductors, pages 98–99. Addison Wesley, 2002.

[28] D. R. Stump G. L. Pollak. *Electromagnetism*, chapter Vector Calculus, pages 30–36. Addison Wesley, 2002.

[29] D. R. Stump G. L. Pollak. *Electromagnetism*, chapter Vector Calculus, pages 14–16. Addison Wesley, 2002.

[30] D. R. Stump G. L. Pollak. *Electromagnetism*, chapter Electrostatics and Conductors, pages 107–108. Addison Wesley, 2002.

[31] D. R. Stump G. L. Pollak. *Electromagnetism*, chapter Electrostatics and Dielectrics, pages 186–187, 191–193, 195–198. Addison Wesley, 2002.

[32] D. R. Stump G. L. Pollak. *Electromagnetism*, chapter Basic Principles of Electrostatics, page 77. Addison Wesley, 2002.

[33] D. R. Stump G. L. Pollak. *Electromagnetism*, chapter Vector Calculus, pages 26–27. Addison Wesley, 2002.

[34] D. R. Stump G. L. Pollak. *Electromagnetism*, chapter Electrostatics and Dielectrics, pages 208–209. Addison Wesley, 2002.

[35] COMSOL. *COMSOL Multphysics User's Guide*, chapter The AC/DC Branch, pages 562–574, 581–598. COMSOL, May 2012.

[36] D. J. Griffiths. *Electromagnetics*, chapter Conservation Laws, pages 351–352. Prentice Hall, 1999.

[37] D. R. Stump G. L. Pollak. *Electromagnetism*, chapter Electric Currents, pages 222–226, 228–230. Addison Wesley, 2002.

[38] COMSOL. *COMSOL Multphysics User's Guide*, chapter The AC/DC Branch, pages 562–568, 574, 598–613. COMSOL, May 2012.

[39] COMSOL. *AC/DC Module, User's Guide*, chapter The Electric Field User Interfaces, pages 133–141. COMSOL, May 2013.

[40] COMSOL. *COMSOL Multphysics User's Guide*, chapter The AC/DC Branch, pages 569–571. COMSOL, May 2012.